Harnessing the potential of CT scanning to identify cryptotephra in sediment cores: a controlled experiment.

Master's Thesis in Earth Science

Quaternary Geology and Paleoclimate

Jan Magne Cederstrøm

Department of Earth Science

University of Bergen

November 2019

Abstract

Volcanic ash (tephra) is a powerful geochronological tool, called tephrochronology, as rapid widespread deposition in multiple environments allows for correlation of geological archives across vast areas. It can thus help to understand the Earth's climate system through time and space, and thanks to analytical advances in the past decades it is now possible to detect invisible (crypto) tephra deposits across thousands of kilometers from its original volcanic source. At present, lab-work related to tephrochronology is both time-consuming and labor-intensive, involving multiple steps to both identify and extract the tephra before it can be analyzed. To overcome these obstacles, we introduce the usage of Computed Tomography (CT) as a tool to identify cryptotephra horizons in sediment cores. The results are promising and show that CT scanning combined with different processing-tools can be used to **1)** locate invisible ash horizons in both minerogenic, ice and organic cores, as well as **2)** visualize the structure of the horizons. Potentially saving researchers a lot of time and further improve the tephrochronological research. The results also highlight the partial volume effect that needs to be accounted for when applying CT scanning on other sediment cores, also outside of tephrochronology.

Acknowledgments

First and foremost, I wish to express my gratitude towards my supervisor Willem G.M. van der Bilt, and my co-supervisors Eivind W.N. Støren, Sarah M.P. Berben, Jostein Bakke and Christine S. Lane. I especially want to thank Willem for coming up with this exiting project, and all the help and input along the way. Also, thanks to Eivind for teaching me how to operate the CT scanner, and EARTHLAB for allowing me to do so, and Sarah for teaching me all I needed to know about tephrochronology. Further I would like to express my gratitude the people the Ice2Ice-project at Bjerknessenteret and Lea Oppedal for allowing me to use your sediment cores in my research. I would also thank Sunniva Rutledal and Johannes Hardeng for all the help and support during this project, and Haflidi Haflidason for providing the Eyjafjallajökull-ash needed for this project.

Thanks to “Det alminnelige naturvitenskapelige forsknings fond” for financial support for my speak at INQUA in Dublin, Ireland.

I also want to thank all my fellow geology students for a great study environment, all the fieldtrips and what’s possible the best social environment you can imagine during all those years, and a special thanks to the guys in “Team Bergen”. Lastly, I want to express my gratitude towards my family for the support through all my years at the University of Bergen, and all the people in Salhus Turn & IL and Laksevåg Turn & IL for allowing me to have the best part-time job ever.

Jan Magne Cederstrøm

Bergen, November 2019

EARTHLAB
Earth Surface Sediment Laboratory

Table of contents

1. Introduction and motivation 1
2. Theoretical background 2
2.1 Tephrochronology 2
2.2 Computed Tomography (CT) 3
2.3 Computed Tomography in geoscience 5
3. Material and methods 6
3.1 Synthetic core design 6
3.1.1 Ice cores 8
3.1.2 Minerogenic cores 9
3.1.3 Organic cores 10
3.2 Application: marine and lake sediment cores 10
3.3 Calibration of CT scans 12
3.4 Grainsize analysis 12
3.5 Core photography 13
3.6 Computed Tomography (CT) scanning 14
3.6.1 CT processing computer 15
3.6.2 CT Processing software 15
3.6.3 Grayscale distribution histogram 16
3.6.4 SplineProbe and statistical analysis 17
4. Results and discussion 19
4.1 Application of calibration cubes 19
4.2 Results of the synthetic cores 20
4.2.1 Ice cores 20
4.2.2 Organic cores 24
4.2.3 Minerogenic cores 27
4.2.3.1 Core containing rhyolitic tephra 27
4.2.3.2 Core containing basaltic tephra 33
4.3 Application on real cores 36
4.3.1 DB2 36
4.3.2 GS15-198-36CC 39
5. Conclusion and implications 45
6. Future work 46
7. References 47

1. Introduction and motivation

Tephrochronology – the use of geochemically distinct volcanic ash (tephra) horizons to date and correlate geological archives – is a powerful chronological tool in Quaternary Geology (Davies, 2015). Following eruptive events, ash plumes rapidly settle within hours to days across vast areas (Stevenson et al., 2012), providing isochronous regional time markers when detected in sediment and ice cores (Blockley et al., 2014).

Over the past decades, new analytical approaches have enabled the detection and identification of smaller invisible ash shards (cryptotephra) at greater distance from their volcanic source (Turney, 1998; Blockley et al., 2005; Hayward, 2011). These advances have greatly expanded existing tephra frameworks across oceans or continents, and further back in time (Lane et al., 2017 and references therein). Progress is, however, held back by the laborious and therefore expensive lab procedures required to extract glass from host sediments. These typically involve a series of flotation procedures with heavy liquids to concentrate tephra shards (Blockley et al., 2005). Often, hundreds of contiguous samples need to be subjected to this treatment to reliably locate cryptotephra horizons throughout records at high resolution (e.g. Smith et al., 2013; Fontijn et al., 2014).

The overall motivation behind this project is to find more efficient ways to identify cryptotephra horizons in geological archives. To do so, we explore the use of Computed Tomography (CT) scanning. As with heavy liquid flotation, this approach characterizes ash based on its characteristic density properties, captured by CT greyscale values. Pioneering work by Griggs et al. (2015) and Evans et al. (2017) highlights the potential of this innovative use of CT scanning to visualize ash in discrete resin-impregnated samples. Here, we further expand this potential by CT scanning entire cores with a unique customized scanner. To do so in a rigorous way, we set up a controlled experiment based on synthetic cores made up of different host materials and spiked with known quantities of tephra shards after Balascio et al. (2015).

2. Theoretical background

2.1 Tephrochronology

Tephrochronology encompasses the use of volcanic ash (tephra) to date and synchronize geological records. Its application has greatly increased over the last decades in Quaternary research because of its potential to substantially improve chronological control (Lowe, 2011). Fundamentally, the application of tephrochronology is based on three principles. First, ash from different eruptions has a unique geochemical fingerprint that allows us to identify and distinguish them. Secondly, it relies on superposition – overlying ash horizons are progressively younger (Feibel, 1999). Finally, it is assumed that ash is instantaneously and synchronously deposited across large areas following volcanic eruptions (Lowe, 2011).

Tephrochronology was first applied by Sigurður Thórarinsson on Iceland in the 1930s (Thorarinsson, 1944). Usage was, at the beginning, only focused on visible tephra horizons in peat (Fig. 1) within close proximity to areas with volcanic eruptions, such as Iceland, Japan and New-Zealand (Davies, 2015). In the 1960s some work was done outside of volcanic areas, but mainly in Scandinavia (Davies, 2015), such as Christer Perssons work on peat bogs in Norway (Persson, 1967). However, it was not until the discovery of microscopic tephra horizons in peat in Scotland in 1989 (Dugmore, 1989) that tephrochronology became a widespread method for correlation and dating outside of Scandinavia (Davies, 2015). Over the past decades, further advances allowed tephrochronologists to find even smaller shards and horizons at increasing distance from their source. Like for example the finding of ash from the North America in Europe by Jensen et al. (2014) (Fig. 2) and the discovery of ash from Kamchatka on Svalbard by van der Bilt et al. (2017), proving that volcanic ash can cross oceans and continents.

Figure 1 - Visible layer of Vedde-ash (arrow) from a peat core close to the Hardangerfjorden. Photo: Bengt Carl Adam Joachim Regnéll

Notwithstanding these advances, the pace of progress is largely set by the labor-intensive and time-consuming

laboratory procedures required to isolate shards (Davies, 2015). Unless researchers target a specific depth interval based on additional chronological data, the entire length of geological archives has to be sampled to assess whether cryptotephra is present (Davies, 2015). For each sample, this process involves more than a dozen steps during which tephra is separated from host material based on the specific density of glass (Blockley et al., 2005).

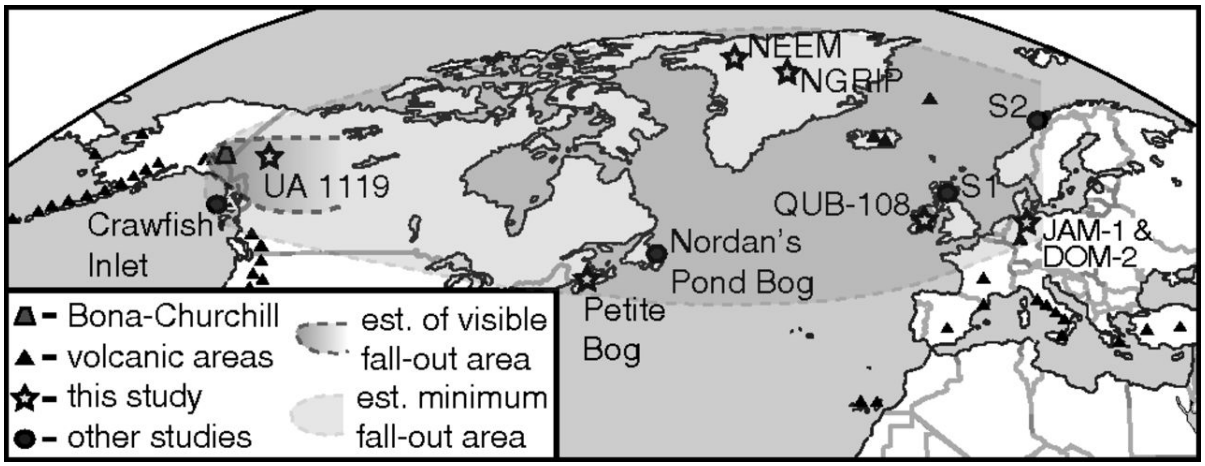

Figure 2 - Site map showing locations of findings (stars/circles) of the White River Ash ranging from Alaska to Norway (From Jensen et al. (2014)).

2.2 Computed Tomography (CT)

Computed Tomography (CT, also sometimes referred to as CAT) scanners use X-ray imagery of scanned objects to compute 3D visualizations based on density differences. Fundamentally, this approach is based on the same principle as röntgen scanning, where an X-ray source (tube) emits radiation that is captured by a detector after attenuation by the sample, which is placed in between the source and detector. The amount of radiation that is absorbed by the sample is calculated based on the number of photons that reached the detector (Hounsfield, 1972). Unlike röntgen set-ups, CT scanners move while scanning; either the X-ray source and detector orbit around samples (e.g. medical CT scanning; Fig. 3A), or the scanned object itself rotates during measurement (e.g. industrial CT scanning; Fig. 3B). Both approaches yield readings from 360 degrees around the scanned object (Hounsfield, 1972), allowing it to be reconstructed in three dimensions (3D). Two different types of scanning exist: *axial* where the scanner just orbits around the object and *helix* where the object also moves through the scanner allowing scanning of longer objects.

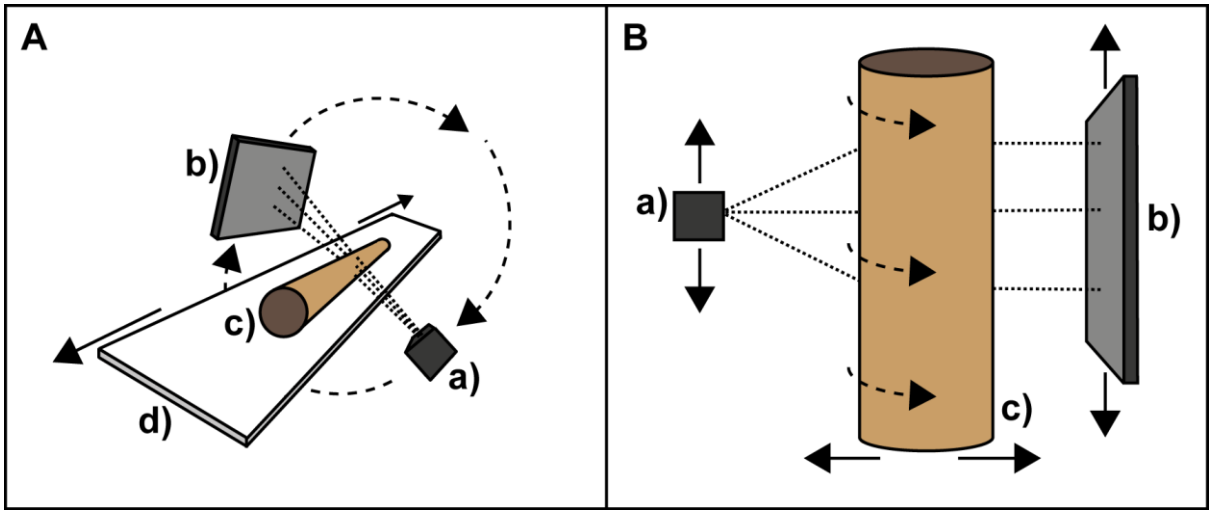

Figure 3 A: Typical setup for a medical CT scanner. B: Example of a setup for an industrial CT scanner. a) Source, b) Detector, c) Sediment core, d) Table in a medical CT scanner. The difference between the setup of scanner A and B is mainly which parts that moves. For a medical CT scanner (A) the source and detector are arranged with a fixed distance between scanned object and source, while for an industrial CT scanner this can often be changed, thus allowing different resolutions for the CT scans.

CT-based visualizations of objects reflect the attenuation of X-ray photons, which is proportional to the density of the scanned material(s) (Kalender, 2011). For example, dense steel attenuates most radiation, while most photons pass through low-density water. In cone-beam based CT systems (like the one used for this project), the degree of attenuation is reflected by grayscale values (Razi et al., 2014). The distribution of grayscale values ranges from black (light) to white (dense), but is unconstrained and depends on the scan settings (e.g. current, voltage) and the scanned object (Bryant et al., 2012). The number of shades of gray depends on the bit depth of the employed scanner: 8-bit scans generate 256 values, whereas 16-bit imagery produce 65 536 shades of gray. This color scale can later be shifted during processing to assign other colors to given values. The resolution of CT scans is typically expressed by the size of the voxels (3D pixels), ranging from micrometers to nanometers depending on the type of scanner and the proximity between the object and source.

2.3 Computed Tomography in geoscience

The usage of CT scanning in geoscience can be traced back to the 1980s when medical CT scanners were mainly used in 1) petroleum geology to measure porosity and permeability (Vinegar and Wellington, 1986), 2) sedimentology to look at structure and fabrics (Renter, 1989) and 3) soil sciences to look at bulk density (Petrovic et al., 1982). In later times the resolution of CT scanners has increased with the new generation of microCT and nanoCT scanners. The application on soft sediment samples, with the scanning of sediment cores, has also increased in recent years. CT scanning has among others been used to look at varves (Bendle et al., 2015), flood layers (Støren et al., 2010), sediment structures (van der Bilt et al., 2018), evidence of past avalanches in sediment cores (Røthe et al., 2019) and bioturbation impact on tephra-depositions in marine sediment cores (Rutledal et al., Submitted).

The possibility for rapid non-destructive visual inspection, and real-time processing are the main advantages of CT scanning in geoscience, as it also allows for multiple calculations done effectively without having to do manual measurements.

3. Material and methods

3.1 Synthetic core design

To explore the possibilities to identify (crypto)tephra using CT scans, we set up a controlled experiment. Specifically, we created a series of synthetic cores that were spiked with known quantities of ash shards after Balascio et al. (2015). To do so, we used 50 ml centrifuge tubes and filled these with alternating layers of sediment and tephra. We added tephra to organic, minerogenic as well as ice cores to reflect the broad range of conditions that is typically found in natural geological archives. We created a set of two cores with each of these materials; one spiked with felsic (rhyolitic) ash, the other with basaltic tephra. These different tephra types cover the typical density range (2-2,5 g/cm^3) of distal volcanic eruptives (Blockley et al., 2005). We used light-colored phonotrachytic ash derived from the 39 ka BP Campanian Ignimbrite (*CI*) eruption as our rhyolitic end-member (Tomlinson et al., 2015), while taking dark-colored basaltic ash from the 2011 CE Eyjafjallajökull (*Ey*) eruption (Dugmore et al., 2013). The color of the ash affected the visibility of horizons in the synthetic cores due to the contrast with the surrounding material.

Both ash types were sieved to ensure that we analyzed size fractions that are most typically used by the international tephra community (Davies, 2015; Abbott et al., 2018). The rhyolitic CI tephra was only sieved with a 25 µm mesh size, owing to its distal sampling location (Romania; ~1000 km). Proximal (Icelandic) basaltic Ey tephra was sieved into the three fractions recommended by Abbott et al. (2018); 25-80 µm, 80-125 µm and >125 µm. We used the intermediate 80-125 µm range for our cores.

Next, we counted shards on a 1 mm^2 gridded picking tray under a Leica MZ6 optical microscope (×40) to determine the approximate number of shards per gram of ash. To do so, we counted and weighed a known quantity of shards – rhyolitic CI and basaltic Ey ash contained 711 400 and 663 500 shards per gram, respectively. Four tephra horizons were subsequently added to each synthetic core at regular (~1.0 cm) intervals, ranging from near-visible (bottom) to diminutive-invisible (crypto; top). We respectively added ~18 000, ~9 000 and ~500 shards to each invisible horizon (from bottom to top) (Fig. 4), while iteratively assessing the visibility of the lowermost horizon per lithology and tephra type. Ensuing shard numbers ranged from 70 000 to 170 000.

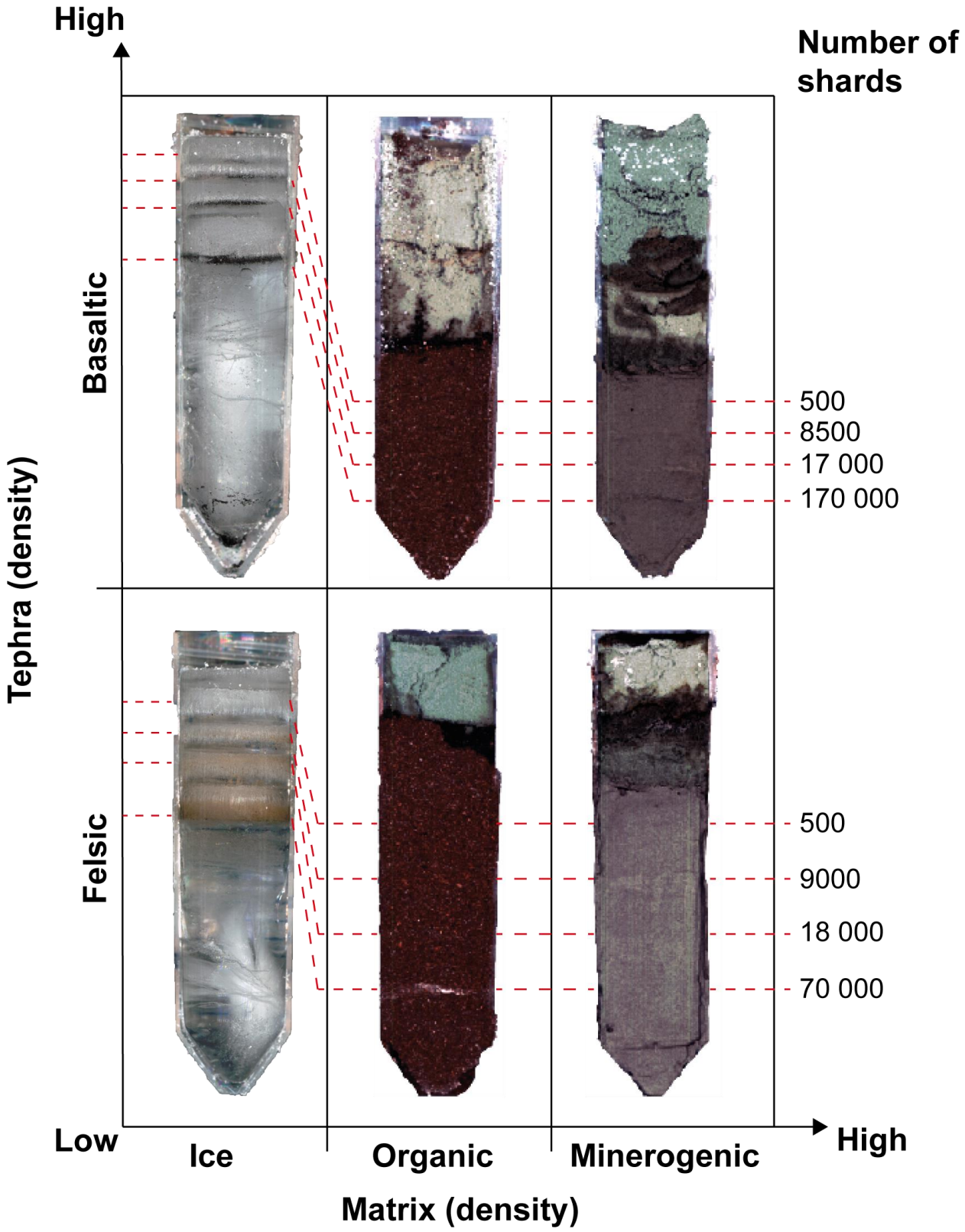

Figure 4 - Overview of the different synthetic cores made for this project, highlighting the different tephra horizons (red dotted line).

3.1.1 Ice cores

Tephra horizons within annually laminated ice cores greatly improves the age estimates for paleoclimate archives, and it is therefore important within the tephrochronological society (Bourne et al., 2015). Thus, it was decided to construct synthetic ice cores to explore if tephra horizons embodied in ice would appear on a CT scan, and also explore the possibilities for CT scanning of ice in a normal environment (not sub-zero degrees). The ice cores also worked as a test-/calibration-scan due to the low-density matrix (ice), which would ensure that the tephra horizon would be easy to detect before applying the method on synthetic cores with a higher density matrix (organic and minerogenic).

To make the synthetic ice cores, distilled water and a commercial freezer set at around -18^{o} C were used. First a layer of ice was made in 50 ml centrifuge tubes by filling 30 ml of water and letting it stand in the freezer until frozen solid. Cold water was then added with a plastic pipette on top of the ice in the test tube, and tephra was sprinkled onto the water letting it sink to the bottom. The test tube was again placed in the freezer, allowing the next layer containing tephra to freeze. This process was repeated for all four tephra horizons in the cores. The layers were placed close to each other in the top part of the centrifuge tube to be able to do axial scans, thus minimizing the scan-time.

To prevent ice melt during scanning, we placed each core inside a foam-isolated 63 mm wide plastic tube that was cooled down by liquid nitrogen. Isolated caps were placed on both ends of the pipe to keep it frozen for as long as possible (Fig. 5). Liquid nitrogen has a gas expansion ratio of 1:694 at room temperature (20°C; Compressed Gas Association, 1999); to ensure safety, we **1**) evaporated most nitrogen prior to capping, and **2**) added valves to release pressure.

Figure 5 - Isolated plastic tube containing liquid nitrogen and the ice core with calibration cube placed on top inside the CT scanner. Photo: Jan Magne Cederstrøm

3.1.2 Minerogenic cores

The minerogenic synthetic cores were made using sediments extracted from deglaciation units within lake cores taken in lake Ingulsjø, Vågå county, located in the southern Norway (61°31′N, 9°01′E 1120 m a.s.l). The source sediments were chosen because of their fine homogenous grain size distribution (clay-sand). The sediments were first dissolved in aqueous (5%) hydrogen peroxide (H_2O_2) to remove all traces of organic material. The sediments were sieved at 63 µm, and only the lower grainsizes retaining the silt and clay fractions were used to limit grading in the sediment during settling.

The synthetic cores were made in 50 ml centrifuge tubes, and the first attempt of making laminated layers was done by using a IEC Centra-4B centrifuge following the method described in Balascio et al. (2015). The method uses the centrifugal force as an alternative to gravity, to allow sediments to settle rapidly. For each layer of the core you add sediments, then run the centrifuge until all of it has settled. The centrifuge was set at 2500 RPM with as little braking as possible. However, using this method, the synthetic cores ended up with tilted layers (Fig. 6). The tilting of the layers could be explained with the limited amount of sediments being used, as tests with larger amounts of sediments in the centrifuge tubes (larger than we could use) solved this problem. As the tilted layers were not ideal for this project, natural settling in distilled water was applied instead. The settling time was set to 30 minutes, based on the time used in the method of separating silt and clay in a wide-mouth glass jar described by Poppe et al. (2001).

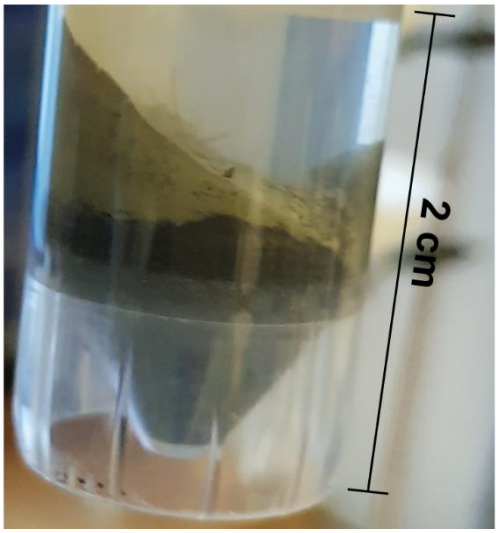

Figure 6 - Tilted layers in the centrifuge tube after using a centrifuge to allow rapid settling of sediments.

Both glass shards and sediments were added by sprinkling it on top of the water, and letting it settle naturally (without help) to replicate a natural environment. To force all the tephra to settle, a few drops of green soap were added to break the water surface tension.

3.1.3 Organic cores

The synthetic organic cores were made with potting soil (made up of peat moss) representing the matrix sediment in 50 ml centrifuge tubes. The first attempt on settling was executed by using the centrifuge similar as with the minerogenic cores. The same problem with tilted layers occurred here. In addition, bigger organic particles would not settle, due to their lightweight and large area to volume ratio. It was also tried to let the material settle naturally in water, but the problem with floating material occurred again. The solution was to make dry cores and using a customized piston to compact each layer.

The (comparatively large) size of potting soil particles also caused the shards to fall in-between the organic material leading to uneven layers. To overcome this problem the compost was homogenized using a grinder for 20 seconds, in order to reach a similar texture as natural organic sediments.

Similar to the synthetic minerogenic cores, a tephra horizon was added by sprinkling it on top of each organic layer. Nonetheless, for the reasons stated above, in these cores no water was used.

3.2 Application: marine and lake sediment cores

In addition to the synthetic cores, two different U-channels taken from real sediment cores were used. Neither of the U-channels were examined for tephra, as they were part of reference-cores, thus the tephra examination was done in other sections of the cores, but at the same depth. The first being a section of the peat core DB2 (95 cm to 120 cm) from a site located on the north-east coast of the sub-Antarctic island of South Georgia (54°13'S, 36°38'W, 16 m a.s.l.) presented in Oppedal et al. (2018). Samples of this core have been previously investigated for their tephra concentrations and the results from that investigation showed a maximum concentration of 300 tephra shards/cm^3 at a core depth of 112 cm. (Table 1) The core was spiked with a thin rhyolitic -tephra horizon in the top part to use for calibration (See section 3.3 and 4.1). The second core-section used was a 41 cm section of the marine core GS15-198-36CC collected during the Ice2Ice-cruise in 2015 (Jansen, 2015). The core was taken in the Denmark Strait, East of Greenland (67°51'N, 21°52′W, water depth of 770 m) (Sessford et al., 2018), and had not been investigated for tephra prior to the scan. Here, the main objective was to investigate whether the results from the scanning could

be used to determine an area of interest for further tephrochronological studies. After the scanning, and processing of the data, a tephra shard concentration profile was manually produced for a section of the core (17-22 cm) by Sunniva Rutledal (Table 2) as part of the Ice2Ice-project.

Table 1 – Tephra in DB2

Depth (cm)	Number of shards/cm^3
95	193
96	37
97	16
98	6
99	2
100	198
101	18
102	33
103	10
104	3
105	5
106	12
107	4
108	5
109	22
110	12
111	9
112	304
113	109
114	13
115	0
116	0
117	10
118	2
119	34
120	2

Table 2 – Tephra in GS15-198-36CC

Depth (cm)	Tephra shards >80 µm pr g
5,5	57
7,5	163
9,5	142,5
11,5	157
13,5	71,7
15,5	111,4
17,5	109,8
19,5	182,6
20,5	323,4
21,5	182,98
23,5	16
25,5	73,9
27,5	17,8
29,5	24,5
31,5	25
33,5	43

3.3 Calibration of CT scans

As outlined in section 2.2, CT grayscale distributions of scanned objects are unconstrained (floating) and depend on the instrument settings and material type (Bryant et al., 2012). Consequently, the grayscale range of tephra likely varies between cores. To remedy this, we tried to calibrate scans with standards. For this purpose, we embedded rhyolitic CI and basaltic Ey ash in 1 cm^3 epoxy molds. These cubes were then placed on top of our synthetic cores during scanning (Fig. 7) to use as guidelines when locating the grayscale values for the tephra horizons. For instance if the tephra inside the calibration cube has a grayscale value of 2000, we would expect the tephra horizons to have the same grayscale value, and thus we could isolate the voxels containing this grayscale value to identify the tephra horizons.

Figure 7 - Calibration cube placed on top of a synthetic minerogenic core containing basaltic tephra prior to scanning. Photo: Jan Magne Cederstrøm

3.4 Grainsize analysis

To check for grading and soft sediment deformation in the synthetic core containing basaltic tephra and minerogenic sediments, grain size distributions were measured using a Mastersizer 3000 laser diffraction instrument with a HydroLV dispersion unit (Malvern Instruments) located at EARTHLAB at the University of Bergen. This was applied after the initial CT scanning on selected cores. Some normal grading was expected, as the grainsize used was within the silt/clay-range, and thus have some difference in grainsize. Soft sediment deformation could potentially create unexpected results or location of the tephra horizons. Prior to the Mastersizer 3000 measurements, Calgon was added as a dispersing agent, and ultrasound was used for 40 seconds. The refraction index was set to 1.543, the absorption index to 0.01 as for quartz, and all samples were measured for 20 seconds at a stirring speed of 2500 rpm. A total of 4 samples was measured over an interval of 0,5 cm and the grain size distribution from each sample was averaged over five measurements to monitor and improve analytical precision.

3.5 Core photography

To be able show the synthetic cores they were split open and photographed using ITRAX XRF Core Scanner from Cox Analytical System (Gothenburg, Sweden) at the Department of Earth Science at the University of Bergen. This resulted in 16-bit photos with a resolution of 1972 x 2906 pixels for the ice cores, and 16-bit photos with a resolution of 1972 x 10095 pixels for the organic and minerogenic cores. No other measurements were taken using the XRF Core Scanner.

3.6 Computed Tomography (CT) scanning

The used CT scanner is a custom-built ProCon CT-ALPHA µCT located at EARTHLAB at the University of Bergen. The scanner is customized for scanning sediment cores vertically. It is equipped with a 3000 x 3000 pixel detector and a 240 kV micro-focus tube, which allows the scanning of cores with a height up to 150 cm and a diameter of 125 mm (CT-Laboratory, 2017) (Fig. 8). Inside the scanner, the core rotates 360 degrees while the detector and tube move vertically along the core, unlike more common medical scanners where the object moves relative to the detector and tube.

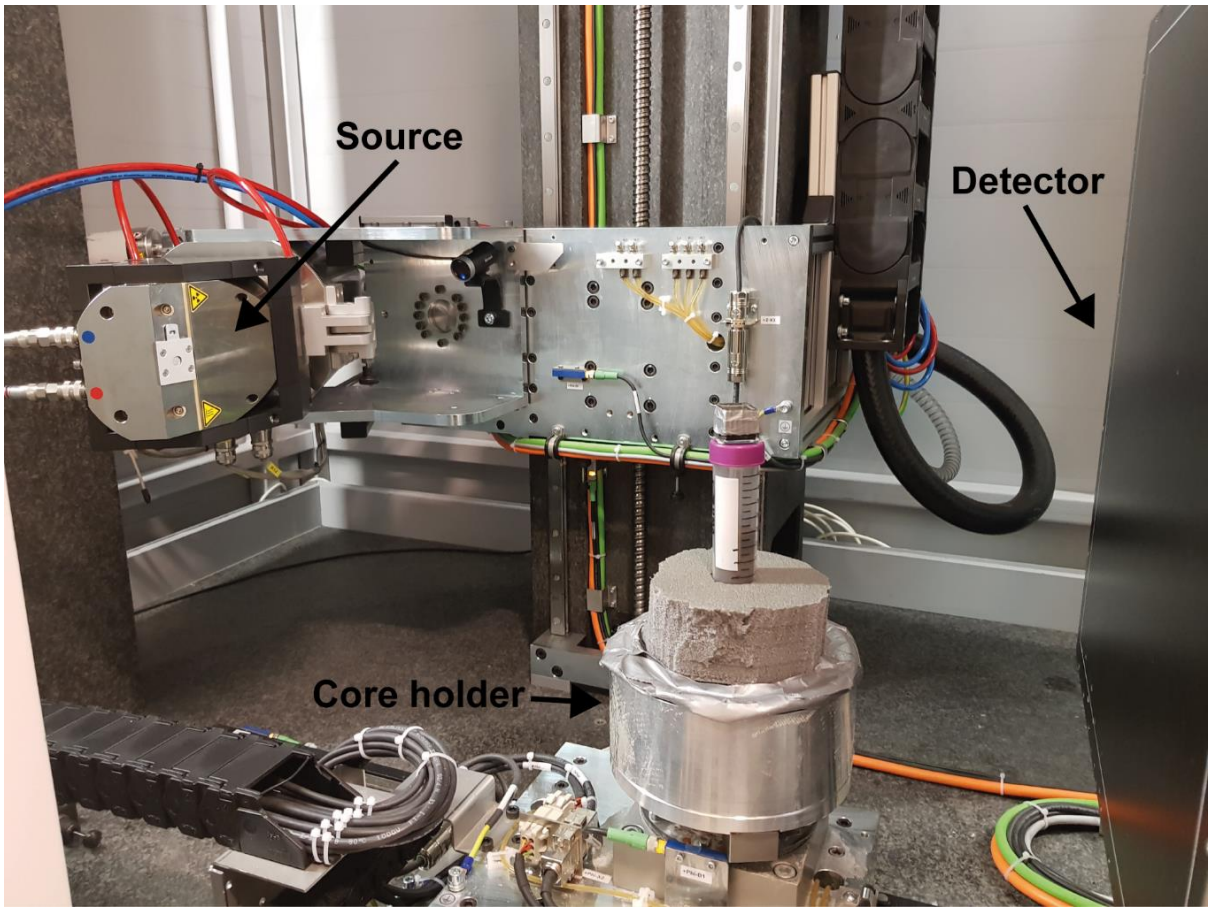

Figure 8 - Setup inside the CT scanner, showing a synthetic minerogenic core containing basaltic tephra placed in the core holder in the CT scanner. During scanning the source will be placed as close as possible to the core holder to allow high resolution scans. Both the source, detector and core holder can be moved inside the scanner. Photo: Jan Magne Cederstrøm

The CT scanning data was reconstructed using the, by Fraunhofer developed, XRayOffice software. The program reconstructs the, from the scanning derived, 2D slices into a three-dimensional (3D) volume by stacking them on top of each other.

For this project, the scanner was consistently operated with a current of 850 µA and a 100 kV voltage, with an exposure time of 267 msec, generating 1600 projections. The

same settings have been used on both the synthetic cores and the U-channels. By using thin objects such as centrifuge tubes and U-channels we have been able to acquire a high resolution on the CT scan (voxel size of 21 µm), opposed to a scan of a full 110 mm core which typically gives a voxel size of around 60 µm due to the increased distance between the source and the detector.

3.6.1 CT processing computer

The computer used for processing the CT data is equipped with two Intel Xeon E5-2620 v4 @ 2.10 GHz processors, 512 GB of Random Access Memory (RAM) and four NVIDIA GeForce GTX 1080 Ti graphics processing units (GPU) (only one used during processing). For this purpose, the RAM has proven to be the limiting hardware, due to the whole CT-data-file being loaded into the RAM. Thus, the file size can not be larger than ~500 GB for the computer used in this project. The file size is determined based on the length, width and voxel size of the core.

3.6.2 CT Processing software

To Thermo Scientific™ Avizo® 9.1.1 suit was used to process CT data and imagery. The tools used for the in Avizo are listed, and specified, in table 3 based on the user guide by Thermo Fisher Scientific (2018), tools are also written in italic in the text. All scanned cores were cut into a 1 x 1 x length (cm) cube before undergoing processing (Fig. 9). This was done to remove the plastic centrifuge tube, limit beam hardening (Brooks and Di Chiro, 1976) and reducing the file-size of the CT data.

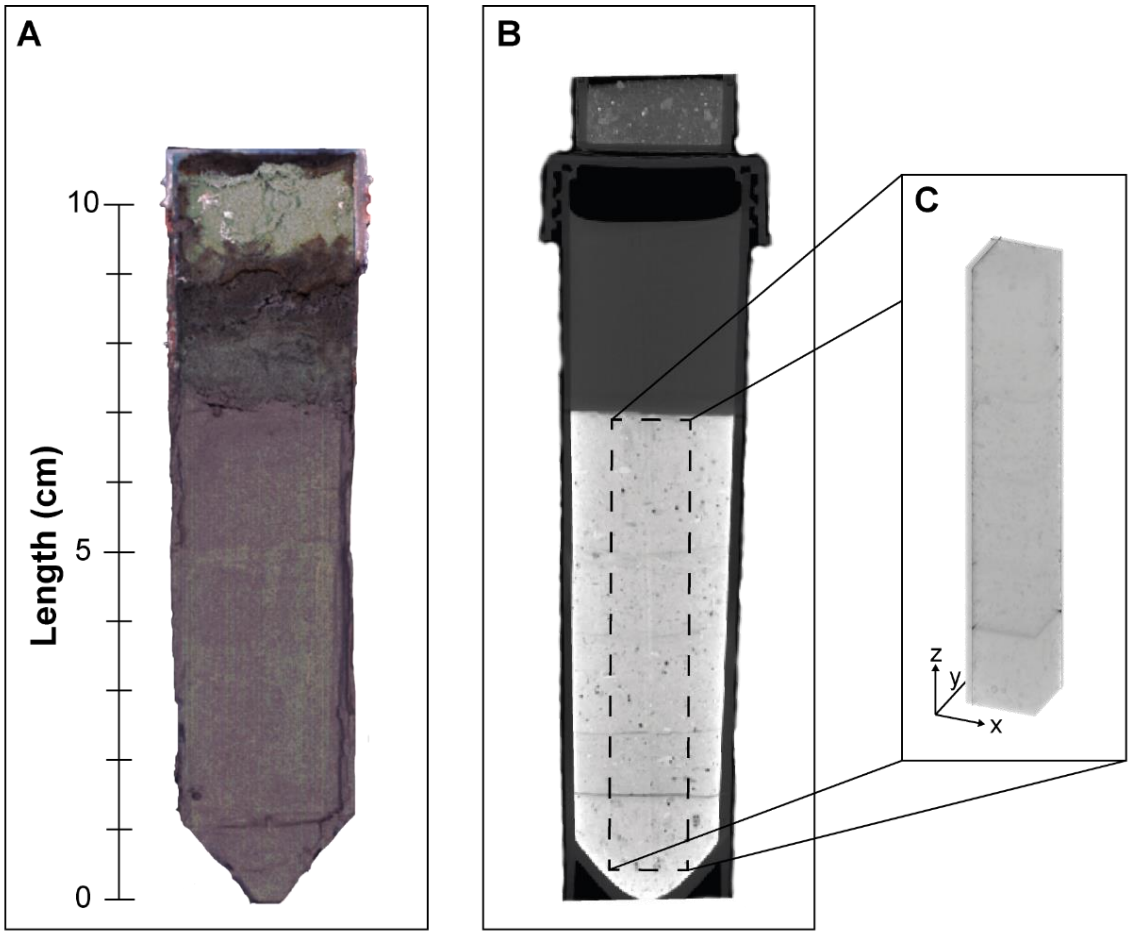

Figure 9 – The progress from core to processing. A) Photo of synthetic minerogenic core. B) Ortho slice of CT scanned core (A) prior to cropping. C) Cropped core section prior to processing.

3.6.3 Grayscale distribution histogram

The voxel values given from a CT scan ranges from 0 to 65 536 (grayscale values) and is often presented as a histogram (Fig. 10), where the Y-axis is the grayscale values and the X-axis is the number of voxels containing each given grayscale value. Thus, the histogram can be used to navigate between different grayscale values (thus, materials) within the scan based on the peaks.

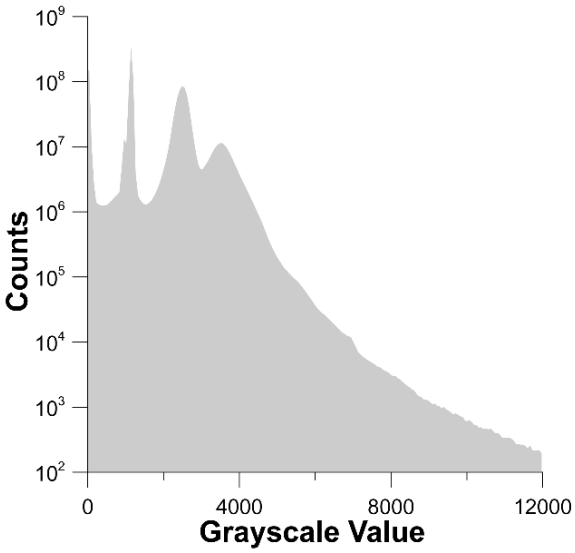

Figure 10 - Grayscale distribution histogram, showing distribution of voxels containing a particular grayscale value.

3.6.4 SplineProbe and statistical analysis

The *SplineProbe* measures the grayscale values at datapoints along a line (table 3). All the *SplineProbe*-data were taken using 500 datapoints along the Z-axis of the core (from top to bottom), averaging the grayscale values within a radius of 0,25 cm from the center of the core. The averaging was done to prevent single elements in the core to affect the measurements. The *SplineProbe*-data were processed and plotted using Python in JupyterLab. First the data were normalized using the Numpy.stat function, this was done as the grayscale values are unconstrained (Section 2.2), and thus it is the difference in value through the core that is interesting. Afterwards the mean and 95% standard deviation was found using the Numpy.mean and Numpy.std functions. It was decided to use the 95% standard deviation as the limit for what would be call a “clear peak”.

Table 3 – Functions and tools used in Avizo (Thermo Fisher Scientific, 2018).

Name	Type	Description
Ortho Slice	Visualization	2D view of the CT scanned object. Can be used on both X-, Y- and Z-axes.
Volume Rendering	Visualization	3D view of the CT scanned object.
Grayscale distribution histogram	-	Visualize the distribution of grayscale values
Interactive Thresholding	Visualization/Data	Creates a binary image of the selected grayscale range.
Spline Probe	Table	Gives the grayscale values along an axis. Can also be used to find the average grayscale values.
Closing	Data	Uses structuring elements to perform a closing matching with a predefined sphere, can thus be used to identify predefined spheres in the data.
Grayscale Reconstruction	Data	Smooths the grayscale into steps.
Auto Thresholding	Data	Separates the voxels in an CT-image into two classes of voxels.
Dilation	Data	Expands all structural elements in a 3D image matching with a predefined sphere.
Arithmetic	Data	Allows the usage of logical or mathematical operations on up to three different input data. The output is given as its own file.
Scalebar	Visualization	Gives the scale of the object in pre-determined unit.
Axis	-	Horizontal axis: X and Y Vertical axis: Z

4. Results and discussion

The required process to identify tephra using computed tomography will be presented and discussed for each core type separately.

4.1 Application of calibration cubes

All the synthetic cores were scanned using a calibration cube filled with the tephra type corresponding to the tephra horizons in the core. The calibration did not work, except for the middle part of some of the thicker horizons, since the grayscale value for the tephra in the calibration cube is higher than for the actual tephra horizons we identify. This happens due to an effect called partial volume effect (sometimes called partial volume rendering), causing smaller volumes (such as thin horizons) to get a lower grayscale value than it originally should have. The effect occurs when the grayscale value does not completely fill a voxel and thus, the voxel overlap several grayscale values. The voxel is then attributed a mixture of the grayscale values (Souza et al., 2005) (Fig. 11).

The calibration cubes worked for detecting the center of the thickest tephra horizons, where the voxels only contained the grayscale value of the tephra and did not get affected by the surrounding matrix.

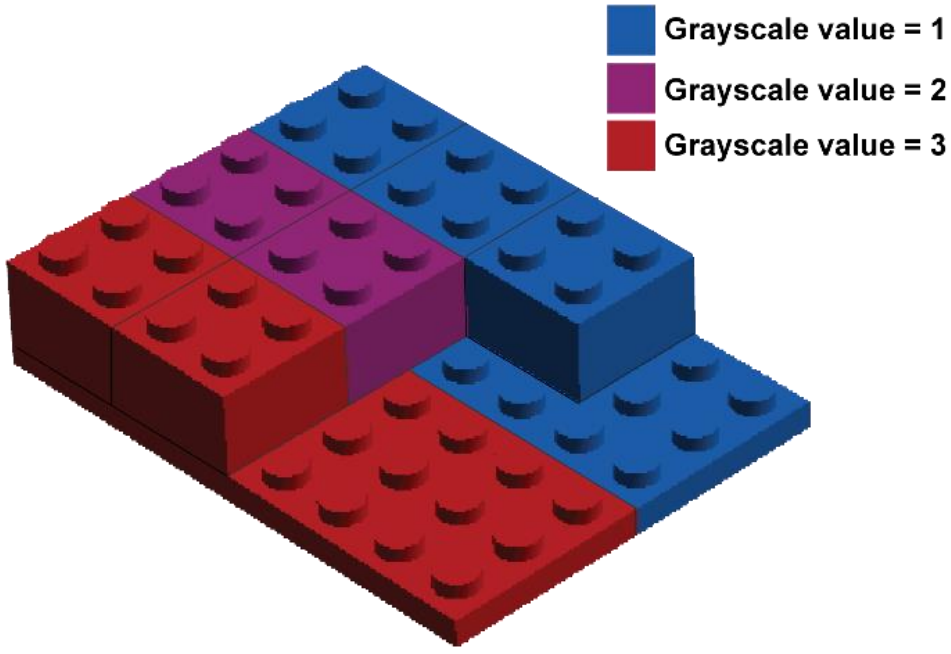

Figure 11 - LEGO bricks used to visualize the partial volume effect that appears when a voxel (bricks) overlaps two areas with different grayscale values (red and blue flat surfaces). The overlapping voxel will then have the average grayscale value of the two underlaying areas. This effect occurs during the reconstruction of the CT-volume.

If the tephra inside the calibration cube had been covered in the same matrix as found in the cores, the transition-area between the tephra and matrix could have been used for calibration. But in this case the tephra was also enclosed in an epoxy with a density of 1,05 g/cm^3 (Biltema Norge, 2017), thus this would not work for us. The approach would also require custom calibration cubes for each individual scan.

To overcome the problem regarding the partial volume effect, we propose spiking the cores by adding a thin layer of tephra near the surface in one of the ends of a U-channel. This was applied on the DB2-core, using a thin layer of rhyolitic CI tephra. Hence the problem regarding the calibration cubes, the synthetic cores was processed using the knowledge about the relative difference in grayscale values between the matrix and the tephra, and the visual structure of the tephra horizons on the volume rendered imagery (Section 4.2.1).

According to Gasser (2003) the partial volume effect causing the problem with the calibration cubes can also be overcome by using a lower voxel size. A lower voxel size would thus limit the total core-length that can be scanned and processed at once (Section 3.6.1).

4.2 Results of the synthetic coresIce cores

It was not possible to replicate natural ice core, since we could neither replicate the snow to ice transformation, nor simulate the ice deformation.

For both synthetic ice cores, the peaks in the histogram were used to determine which part of the grayscale values corresponded with ice. This was done by changing which grayscale values were visible in the *Volume Rendering*. Further, we know from Blockley et al. (2005) that tephra has a higher density than ice and thus, a higher grayscale value for tephra compared to that of ice was expected. The tephra was thus identified by visually highlighting only the grayscale values higher than those of ice.

As seen in both figure 12, 13 and 14, the tephra clusters together on the CT imagery, and it is not possible to determine individual shards in neither of the two tephra types. But when the tephra-shards are clustered together on the CT imagery, the volume rendered imagery gives another texture for the tephra horizons than other objects we have observed (Fig. 12). This can potentially be used to locate tephra horizons on CT scans.

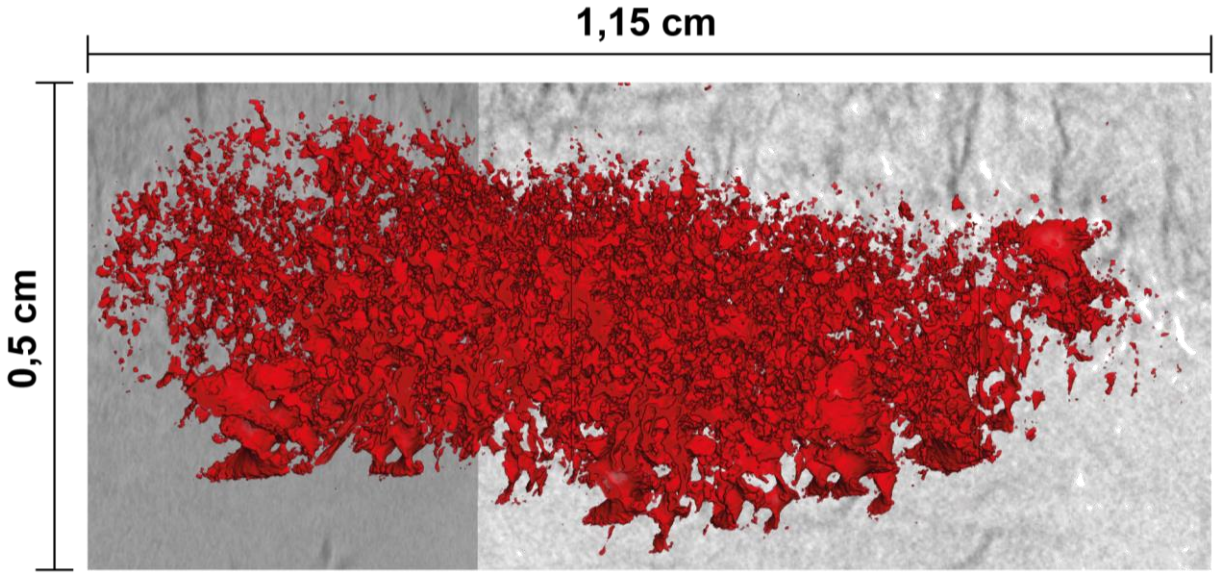

Figure 12 – Volume Rendering of the thickest basaltic tephra horizon within the synthetic ice core. The tephra clumps together and forms a unique structure compared to e.g. silt or ice.

After the initial localization of the tephra, the *SplineProbe*-tool (Section 3.6.4) was applied on both cores to detect density anomalies in the ice associated with the tephra horizons.

When analyzing the *SplineProbe*-graph for the ice core containing basaltic tephra (Fig. 13), it shows one clear peak (~0,8 cm) and an area with multiple peaks (1,5-2,0 cm). There are also some smaller peaks upwards in the core (3 and 4 cm). Due to the tephra being dispersed vertically in the ice, none of the peaks are very abrupt. Based on the CT imagery and visual examination, the vertical spreading seems to be due to cracking, melting of the ice and some tephra frozen into the ice before it has sunken to the bottom. The last part can be seen clearly by looking at the top of the core (5 cm), where a thin layer of tephra has formed due to the surface tension of the water. It is therefore reasonable to believe that this could have happened for the other horizons as well.

The one clear trough in the *SplineProbe*-graph at ~4 cm is due to a glitch in reconstruction leading to a missing *Ortho Slice* in this area.

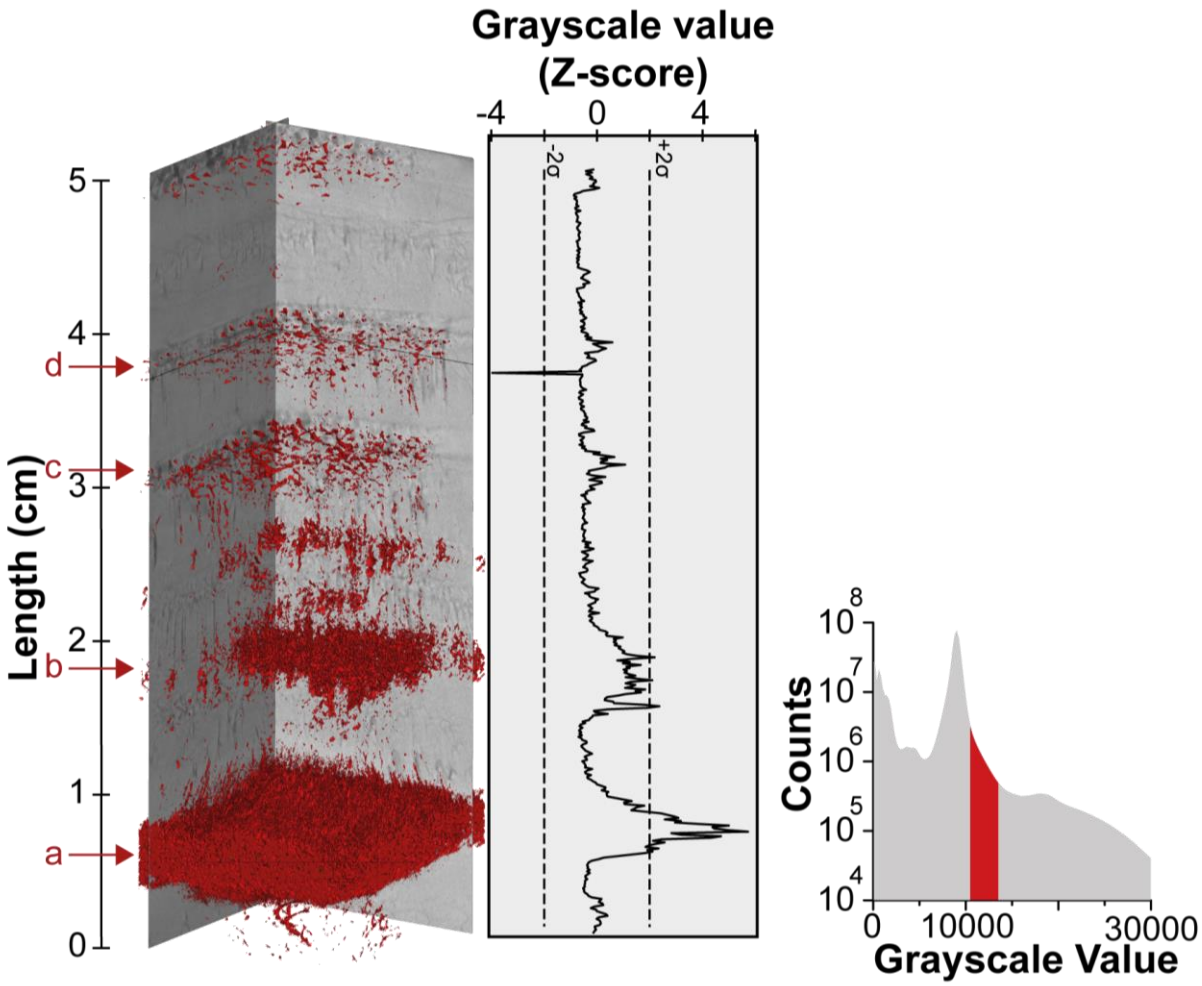

Figure 13 - Volume Rendering of the basaltic tephra (red) in a synthetic ice core. Letter a-d marks the tephra horizons. The SplineProbe-graph shows the normalized grayscale values downwards in the core. The graph shows clear peaks for layer a and b, but only small peaks for layer c and d, whereas the Volume Rendering is able to visualize all four layers. The fifth layer seen on top (5cm) is due to floating tephra that has been frozen before it settled.

For the synthetic core containing rhyolitic tephra, the *SplineProbe*-graph provides little info (Fig. 14). This is due to even more dispersing of the tephra in the ice than in the basaltic core, leading to no clear transition between ice and tephra. The clear troughs in the upper part of the *SplineProbe*-data is most likely due to cracks in the ice. Here, the higher grayscale values compared to the air at the top of the core are due to the partial volume effect (Section 4.1).

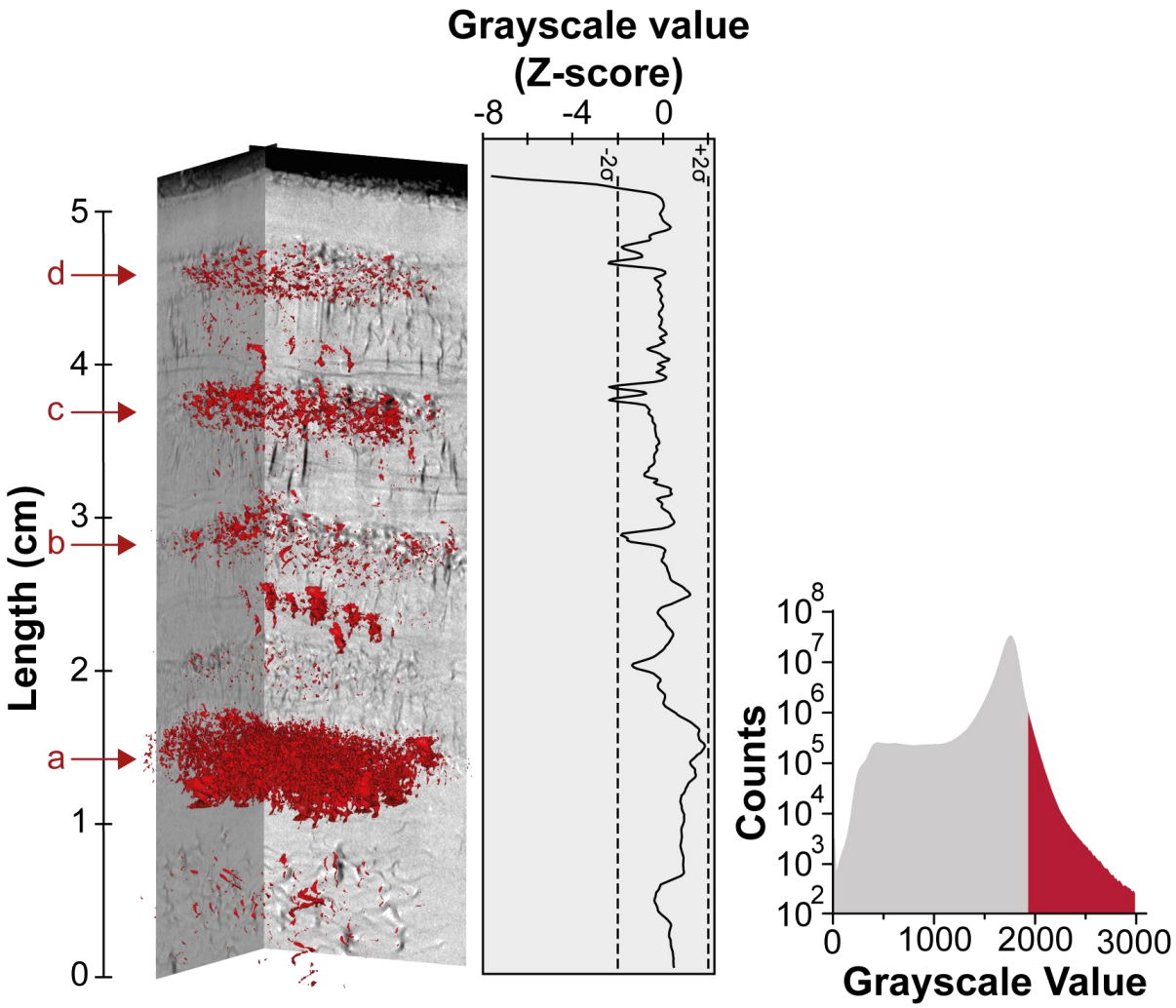

Figure 14 - Volume rendered imagery of the rhyolitic tephra (red) in an ice core. Letter a-d marks the tephra horizons. The SplineProbe-graph shows the normalized grayscale values downwards in the core. No clear peaks can be seen in the graph due to the vertical displacement of the tephra creating a higher average grayscale value than normal. The troughs are due to voids of air in the ice due to cracking. The Volume Rendering is able to visualize horizon a-d, and also shows the vertical displacement.

As seen on both the volume rendered imagery and the *SplineProbe*-data for both cores, the tephra has been dispersed vertically and is not seen as complete horizontal horizons. The *SplineProbe*-tool relies on difference in grayscale values along the Z-axis, thus the vertical dispersal of the tephra makes it hard to use. We must then rely on *Volume Rendering* of pre-determined grayscale values; based on either **1)** calibration-horizons or **2)** the known grayscale values of the ice (thus, the tephra will have a higher grayscale value).

4.2.2 Organic cores

Both synthetic organic cores were first processed the same way as the ice cores, using the histogram and *Volume Rendering* to identify the tephra horizons. To identify the tephra horizons the grayscale value for the matrix (organic material) was first identified using *Volume Rendering* and isolating the main peak in the histogram (grayscale values of ~3000). From Blockley et al. (2005) it is known that tephra has a higher density than the organic material, thus a higher grayscale value. Therefore, the tephra horizons were identified by *Volume Rendering* isolated grayscale values with a higher grayscale value than the matrix. As with the ice cores the identification process was done by visual inspection of the volume rendered data (horizontal lines), and the identification was helped with the knowledge of where the different horizons were located. For the synthetic core containing basaltic tephra the partial volume effect (Section 4.1) proved to affect the horizons, as the middle of the thickest horizon (a in Fig. 15) had a higher grayscale value compared to the rest of the horizons. Due to the higher grayscale value of basaltic tephra compared to that of the matrix, tephra horizons were easier to visualize in the basaltic core (Fig. 15), than it was within the rhyolitic core (Fig. 16).

In both the rhyolitic and basaltic core, a lot of high-density artifacts were scattered around. These artifacts are most likely the result of chalk (density of 1,9-2,8 g/cm^3 (Engineering ToolBox, 2009)) added to the organic material by the manufacturer. The artifacts have a grayscale value in the same range as the tephra, proving visualization of the thinner tephra horizons hard.

The *SplineProbe* was applied to both cores and showed two clear peaks in both cores (0,5 cm and 1,5 cm in Fig. 15 and 0,8 cm and 2,1 cm in Fig. 16). These peaks align with the location of the two thickest tephra horizons in both cores. The smaller horizons in both cores (horizon c and d in figure 15 and 16) were not possible to detect using the *SplineProbe.* This is most likely due to the artifacts in the cores creating an average grayscale value which were the same as the average grayscale value created by the thin tephra horizons. If the matrix had not contained high density artifacts, it would most likely be possible to detect the thinner horizons using the *SplineProbe*.

As seen by the appearance of the chalk in the synthetic organic cores, high density material (such as sand) can create difficulties regarding the usage of CT scanning to

identify thin tephra horizons in organic sediment cores. Thus, this must be taken into consideration when using CT scanning to try to identify tephra horizons.

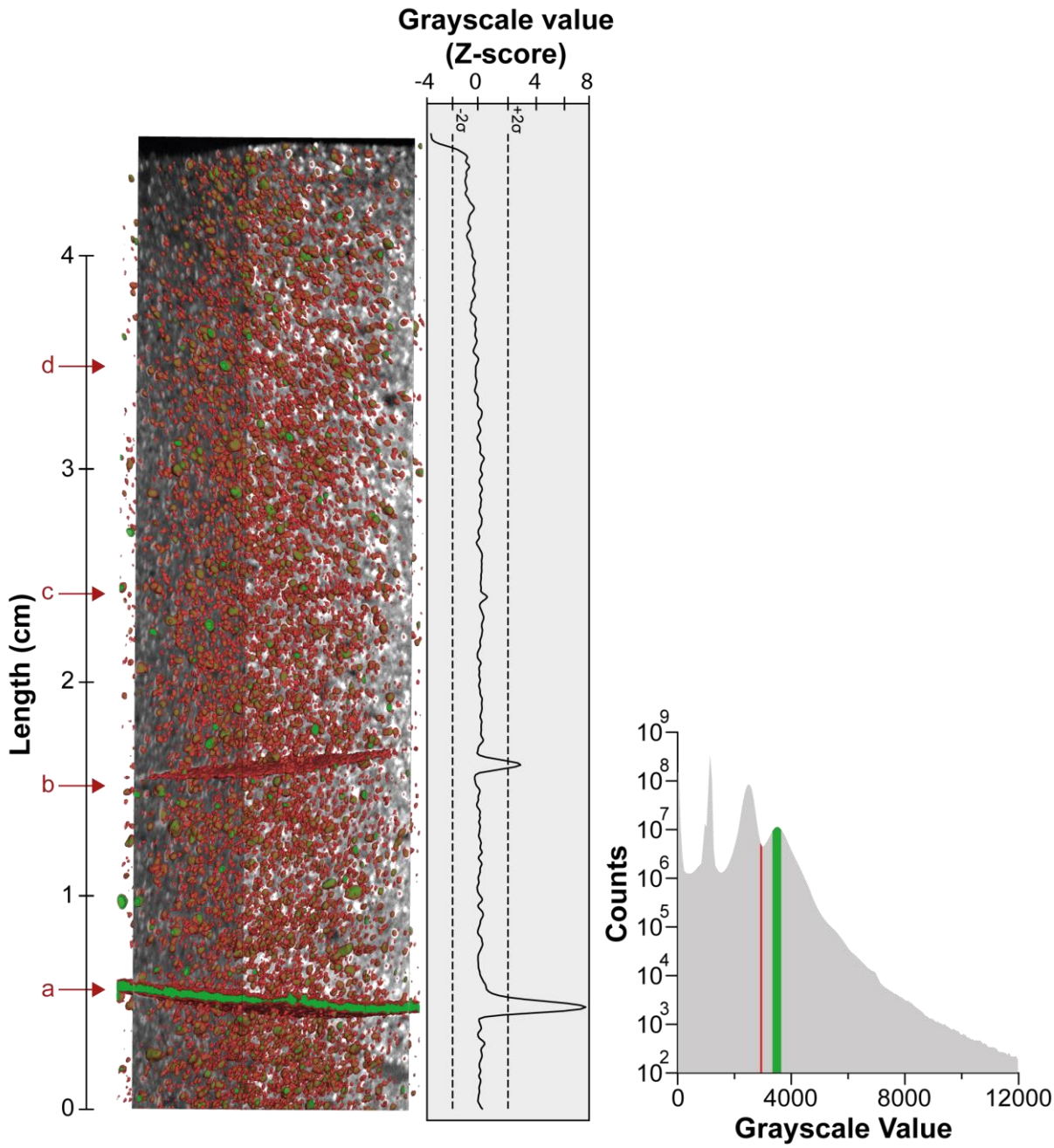

Figure 15 – Synthetic organic core containing basaltic tephra. Letter a-d marks the tephra horizons. The red and green Volume Rendering visualizes the tephra horizons, as well as lots of artifacts in between the horizons. Due to the artifacts only horizon a-c is possible to visualize. Middle of horizon a have a higher grayscale value than the rest of the horizons since it is not affected by the partial volume effect. The graph shows the normalized SplineProbe-data within the core. The SplineProbe-graph shows clear peaks of the two thickest horizons (a and b).

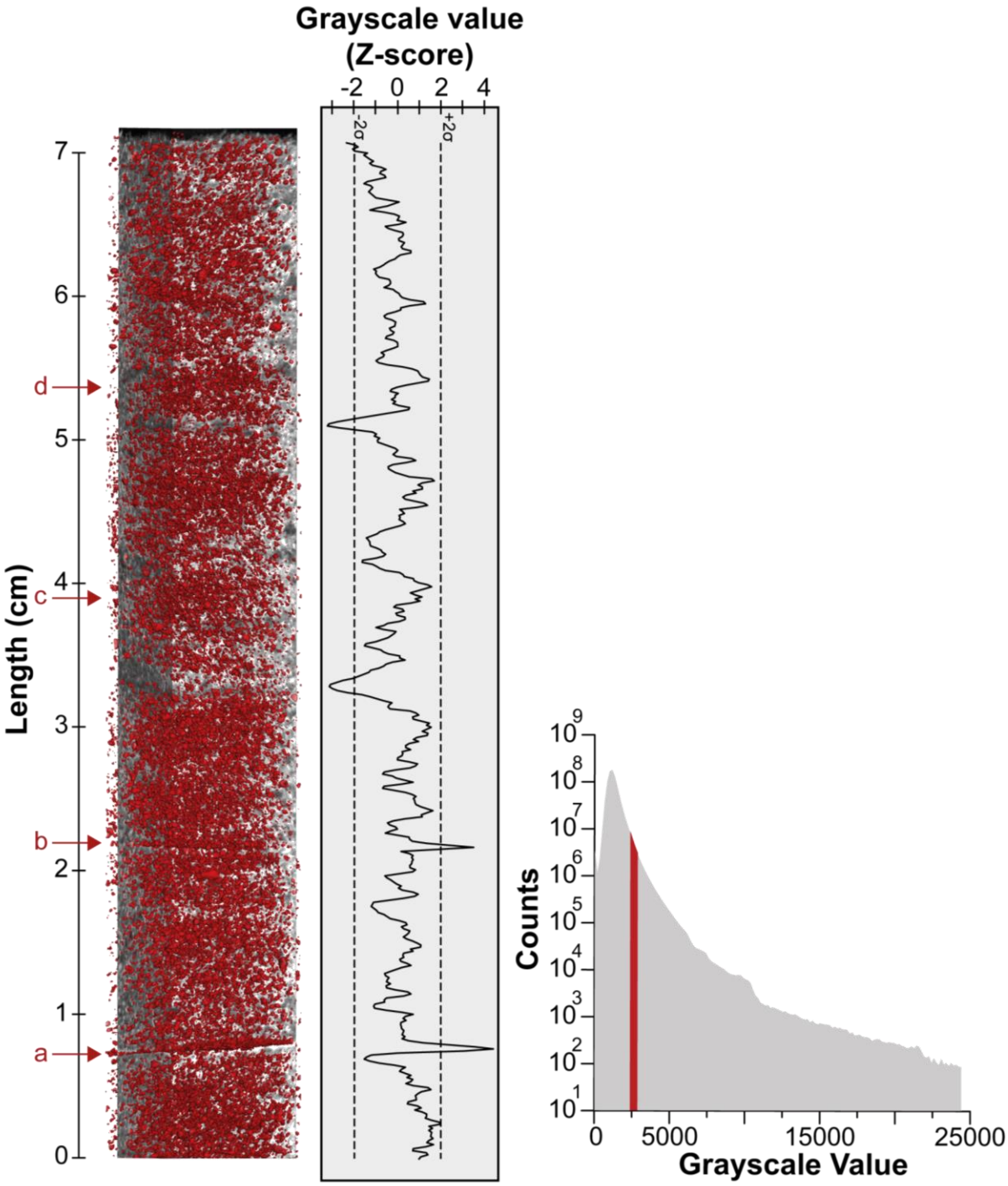

Figure 16 – The synthetic organic core containing rhyolitic tephra. Letter a-d marks the tephra horizons. The red Volume Rendering highlights the tephra horizons, as well as the artifacts with the same grayscale value. The graph shows the normalized SplineProbe-data within the core. Both the SplineProbe-graph shows clear peaks for the location of the two thickest horizons (a and b), these can also be seen on the volume rendered imagery.

Based on the chalk artifacts inside the synthetic cores it was decided to also apply this approach on the DB2-core (Section 4.3.1), which we know have a previously identified tephra horizon (Section 3.2).

4.2.3 Minerogenic cores

The two synthetic minerogenic cores were processed in the same way as the organic and ice cores. However, the difference in grayscale values for the rhyolitic and basaltic tephra relative to the matrix makes the processing of the minerogenic cores more complicated. Thus, the processing has been divided into two subsections, one for each type of tephra, respectively.

4.2.3.1 Core containing rhyolitic tephra

Manual processing using the histogram and the *Volume Rendering* to highlight tephra horizons proved to be the most effective. This was done by first identifying the matrix (silt/clay) and then locating the tephra horizons. Based on Blockley et al. (2005), it was known that the rhyolitic tephra had a slightly lower density than the matrix, thus a lower grayscale value. The horizons were therefore located by *Volume Rendering* of only the grayscale values around 2-2500 (Fig. 17), whereas the matrix was located at the grayscale values ranging from ~2700 to 4000.

The *SplineProbe* will not show any peaks for the rhyolitic tephra embodied in a sediment matrix, since the tephra have a lower density (thus, lower grayscale) than the matrix. Thus, we would have to look for troughs. For the *SplineProbe*-data of our synthetic core (Fig. 17), two clear troughs are visible. One located at ~1 cm and one at ~4 cm. The first one is due to the thickest horizon containing 70 000 shards (horizon a), and the second one is for the horizon containing 9 000 shards (horizon b).

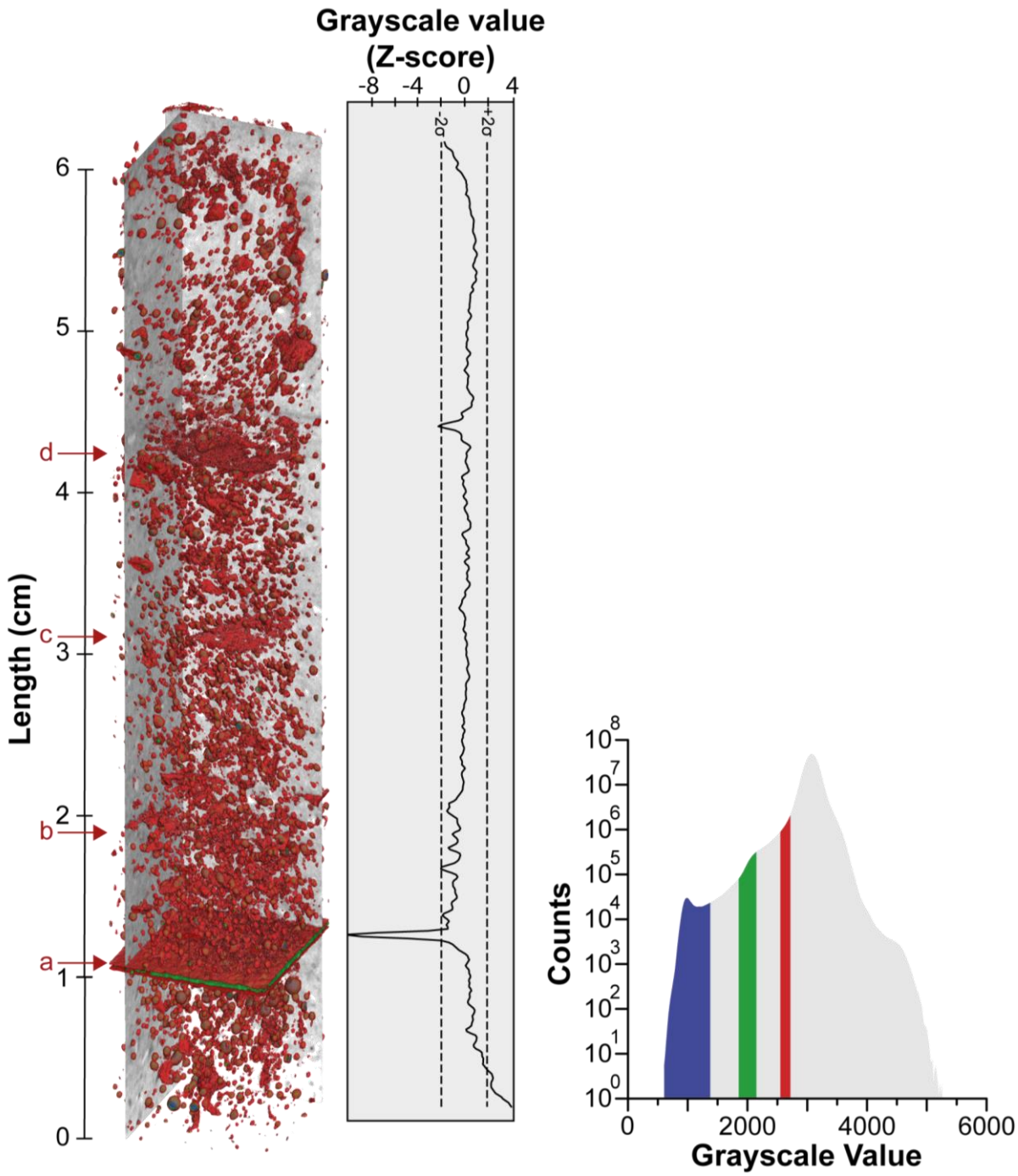

Figure 17 – The synthetic minerogenic core containing rhyolitic tephra (red and green) with the porosity highlighted with blue interior. Letter a-d marks the tephra horizons. Unlike the other cores, the rhyolitic tephra has a lower grayscale value than its surrounding matrix. The graph shows the normalized SplineProbe-data, whereas only horizon a and d can be seen as a clear trough. The Volume Rendering allows visualization of all four horizons (a to d). The middle of horizon a have a lower grayscale value since it is not affected by the partial volume effect.

For the synthetic minerogenic core containing rhyolitic tephra the thinner horizons (horizon b, c and d in figure 17) and the outer parts of the largest horizon (horizon a in figure 17) gets affected by the partial volume effect (Section 4.1). While for the middle of horizon a the partial volume effect does not apply. Thus, the partial volume effect

causes the middle of the thickest horizon to have a lower grayscale value than the other horizons since the voxels here only contain the real grayscale value of the tephra.

As seen in figure 17 the core is filled with porosity (round clasts with green and blue interior) that gets visualized together with the rhyolitic tephra horizons. The porosity gets visualized with the tephra horizons since the transition area between the porosity and the surrounding sediments have the same grayscale value as the tephra horizons (Fig. 17). This is caused by the partial volume effect (Section 4.1) which affects the edges of the internal porosity in the sediment core. Hence the horizons will be obscured due to the porosity in the sediment core. This will only appear in a minerogenic core with rhyolitic tephra since the grayscale value of the rhyolitic tephra is located between grayscale value of porosity and silt/clay. In the synthetic sediment cores the porosity is higher than it normally would be, which is most likely due to the lack of pressure (low water column) and short time between settling of the sediment and the CT scanning. The porosity challenge caused by the partial volume effect can be sorted using either the porosity-extraction method described under, based on Thermo Fisher recommendations (P. Westeberg, pers. comm.) or by looking at the shape (roundness) of the porosity while highlighting the interior of the porosity in a different color (see figure 17).

The porosity-extraction method consists of multiple steps and aims to remove the porosity from the volume rendered imagery using the grayscale values and shape of the porosity, and the full method as seen in “Project View” in Avizo is showed in figure 18, and all tools written in *italic* is also described in table 3. Before the porosity can be eliminated using this method, the grayscale values of the edge between porosity and sediments, as well as the grayscale value of the tephra must first be identified. Then the first step of the method is running the *Closing*-tool as “precise” with an approximal size of 8 (depending on size of porosity) and set the type to “ball”, this will identify all the round spheres in the *Ortho Slices.* Afterwards use the *Grayscale Reconstruction-tool* by attaching the original file as “Input A” and the *Closing*-results as “Input B”, this will smooth the grayscale into steps. On the result from the *Grayscale Reconstruction* run *Arithmetic* with the result as “Input A” and the original file as “Input B”, setting the equation to “A-B”. Next, run *Auto Threshold*, with default settings, on the result from the *Arithmetic*. *Auto Threshold* separates the voxels into two classes. The next step is to run *Dilation* as “precise” on the result from the *Auto Threshold*-tool, with the size set

at approximately 8 (same as *Closing*) and the type set to “ball”. Figure 19 shows the result after this step, when it has been visualized together with the original *Volume Rendering*. To remove the porosity from the imagery, the original file must first be transformed into a binary-file using *Interactive Thresholding*, with the threshold set to the grayscale values of the tephra. Then, to extract the porosity from this imagery run *Arithmetic* with the result from the *Interactive Thresholding* as “Input A” and the result from *Dilation* as “Input B” with the equation set to “A-B”. Lastly, *Volume Rendering* of the final result from the *Arithmetic* will give a figure where most of the porosity has been removed (see Figure 20).

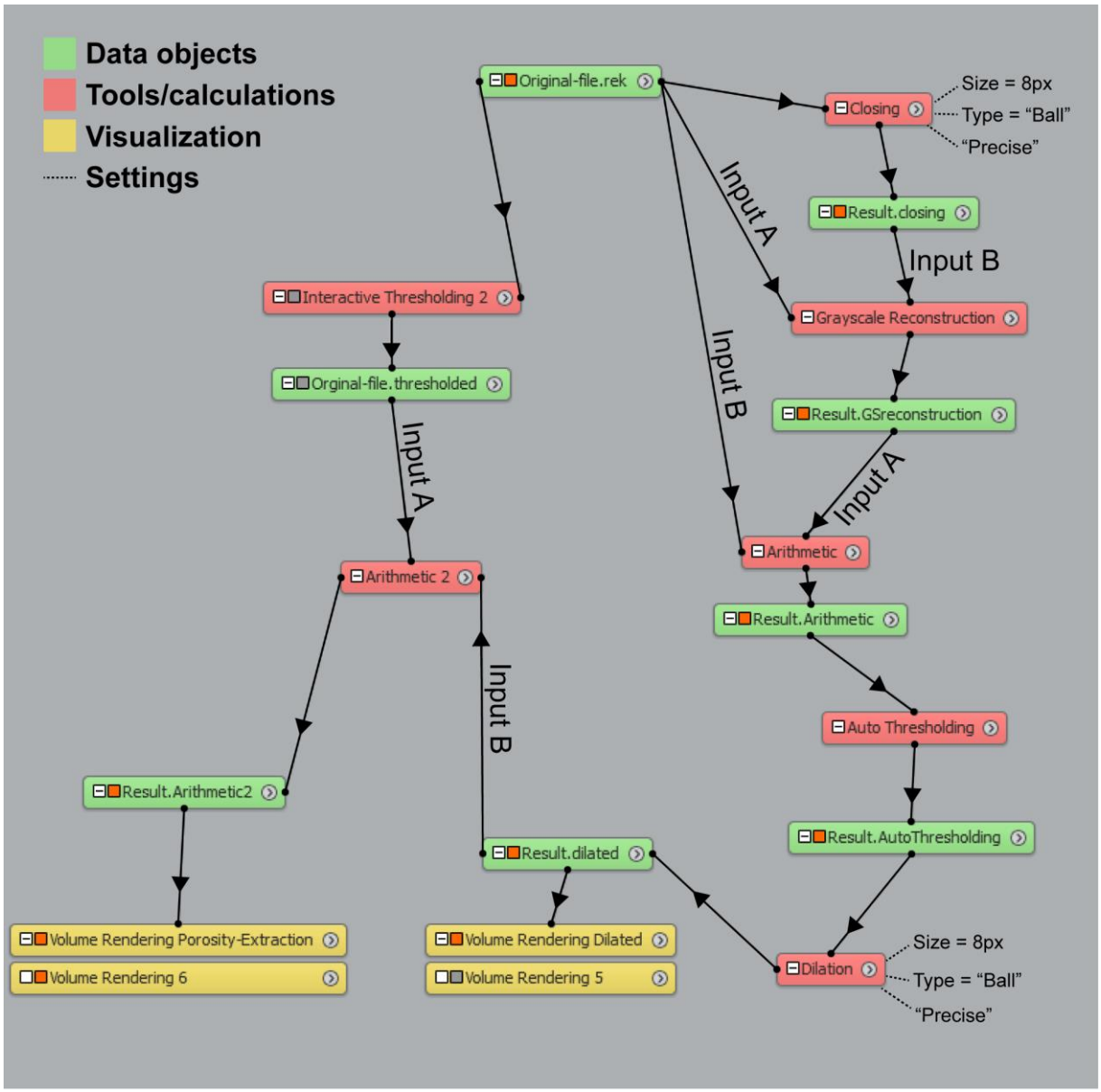

Figure 18 - The porosity-extraction method as seen in the Project View in Avizo. The final result (Fig. 19) is visualized by the “Volume Rendering Porosity-Extraction”, while figure 18 is visualized by the "Volume Rendering Dilated". All settings and inputs have been manually added to the figure.

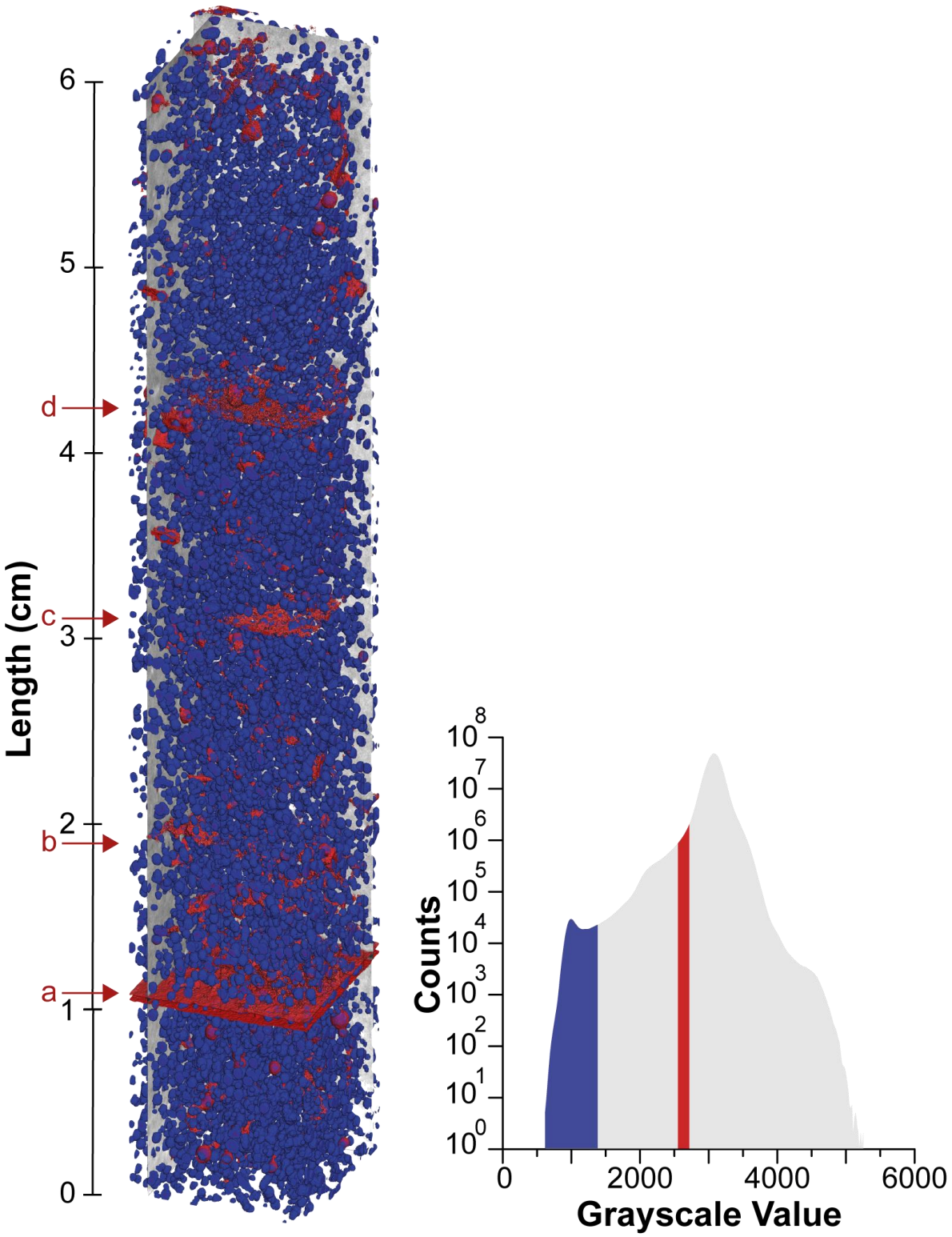

Figure 19 - The result after isolating the porosity (blue), using the porosity-extraction method, overlaying the original volume rendered image (red). The imagery seems to contain more porosity than the original, this is due to all the small porosity being expanding during the Dilation-part of the Porosity-Extraction method.

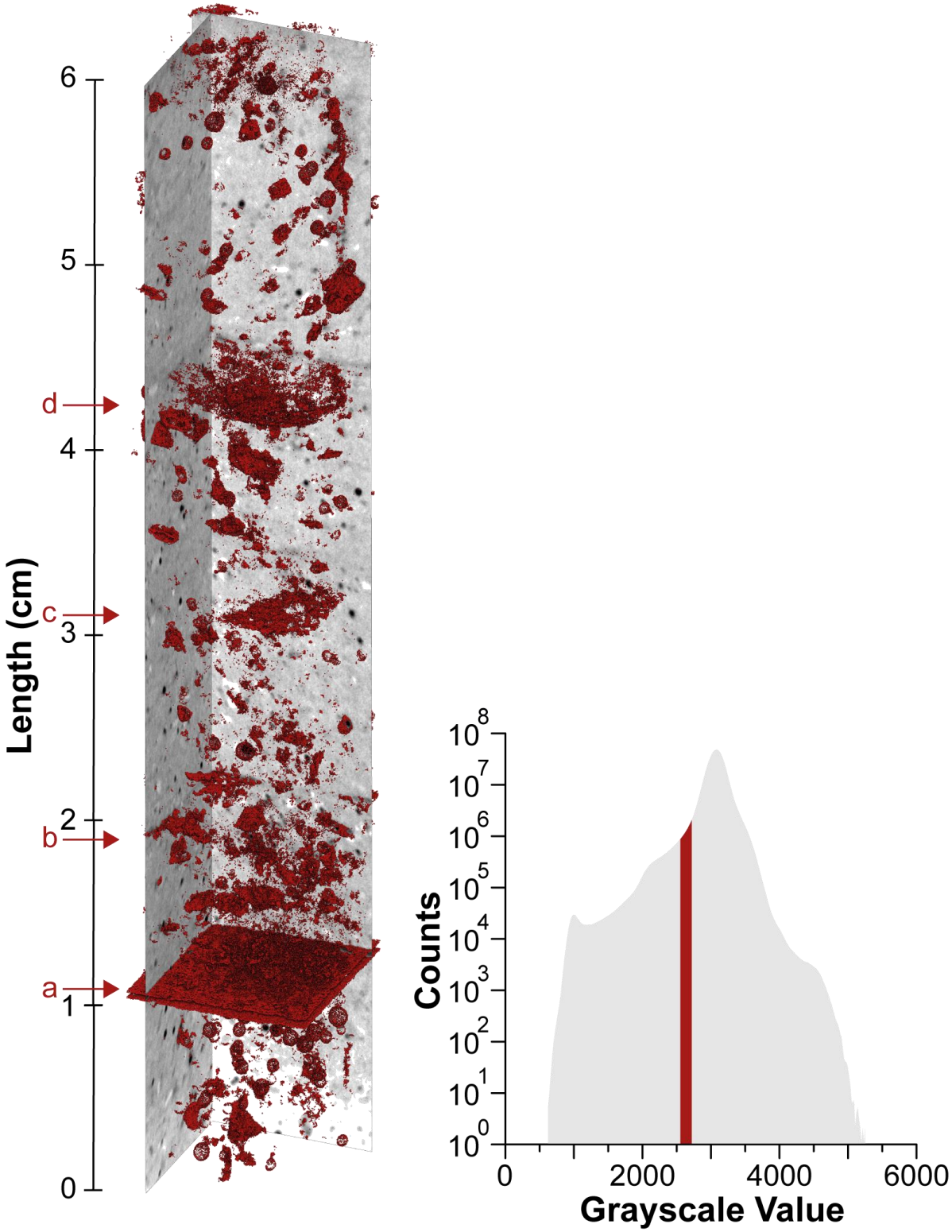

Figure 20 – Final result after applying the porosity-extraction method on the synthetic minerogenic core containing rhyolitic tephra. Here porosity has been subtracted from the original volume rendered imagery based on its shape, and we are left with the tephra horizons. As seen the method has not been able to remove all the porosity (e.g. 2,5 cm).

Since the process to remove the porosity is time-consuming, and the porosity can easily be spotted based on the shape (roundness), and the low-density interior (Fig. 17). It is not recommended to use the porosity-extraction process if the sole purpose is to locate tephra. If the purpose is to create figures to use outside of Avizo, this could be a good way to visualize the horizons more clearly.

4.2.3.2 Core containing basaltic tephra

The synthetic minerogenic core containing basaltic tephra underwent the same processing as the other synthetic cores regarding visualization and the use of *SplineProbe*. The *Volume Rendering* was done based on the grayscale distribution histogram (Fig. 21), where a peak to the right of the matrix contains the real grayscale value of the basaltic tephra (Fig. 21; green). Due to the partial volume effect, the thinner horizons (a, b and c in figure 21) have a slightly lower grayscale value than this (Fig. 21; red). The *Volume Rendering* is able to visualize horizon b (17 000 shards) and c (8500 shards) in the core, while horizon d is absent (Fig. 21).

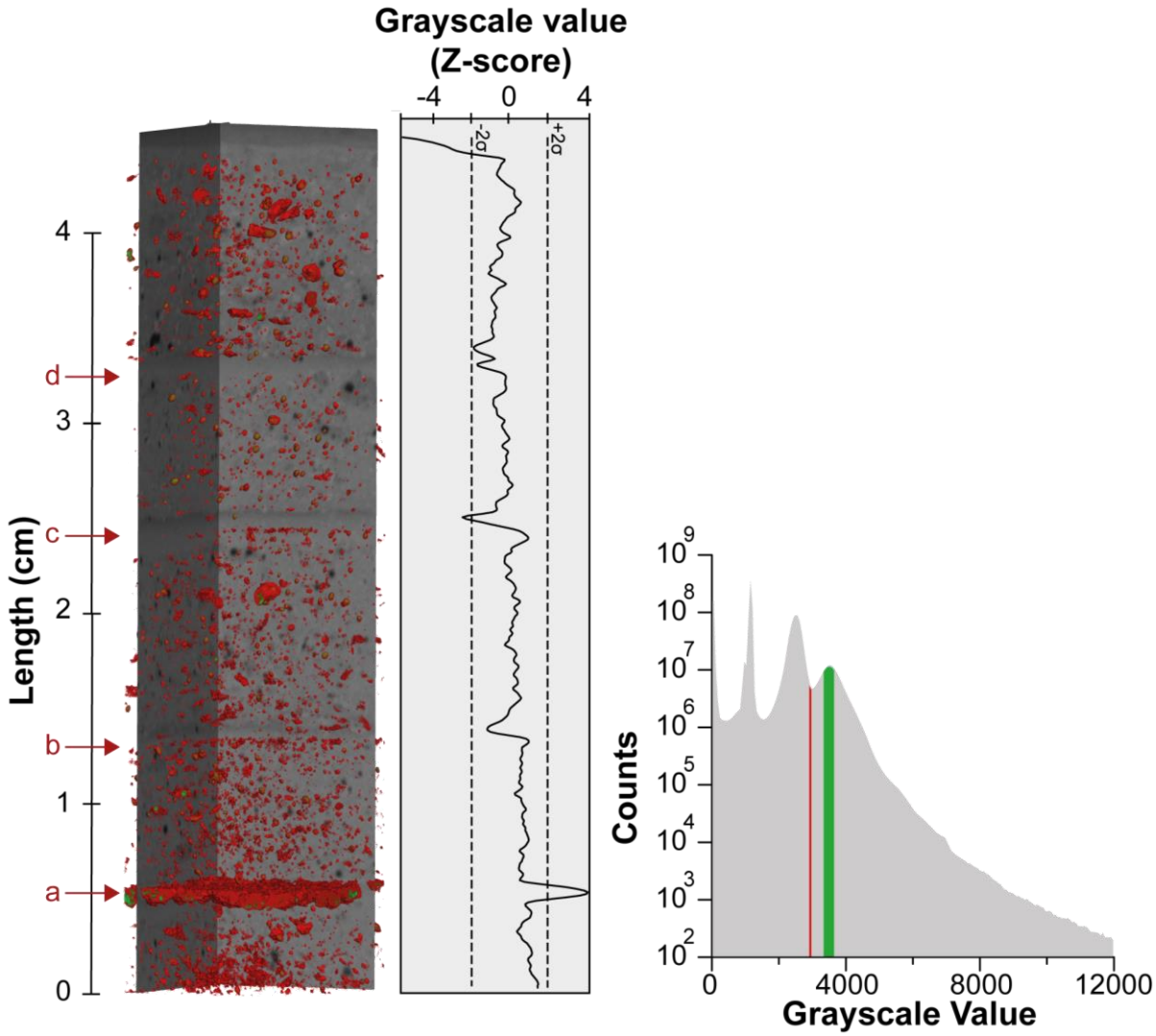

Figure 21 – The synthetic minerogenic core containing basaltic tephra (red and green). Letter a-d marks the tephra horizons. The graph shows the normalized SplineProbe-data and shows only one clear peak (horizon a). The troughs in the SplineProbe-graph is due to areas of low-density material such as wet clay. The wet clay has led to soft-sediment deformation, leading to a vertical spreading of the basaltic tephra, thus horizon b to d is harder to see compared to horizon a. The matrix also contains some high-density material with a grayscale value within the range of tephra, thus making it even harder to locate the tephra horizons. The middle of horizon a is not affected by the partial volume effect, thus getting a higher grayscale value than the other horizons (green).

The *SplineProbe*-data for this core shows only one clear peak related to the thickest horizon (170 000 shards, horizon a in figure 21), but no clear peaks for the three remaining horizons are recorded (horizon b, c and d in figure 21).

As seen in figure 21, and further visualized by the *SplineProbe*-graph (troughs), the core contains multiple low-density layers (at ~1,5 cm, ~2,5 cm and ~3 cm) most likely containing fine material. The layers are located on top of the tephra-horizons, where there normally would be coarser material due to the normal grading. We suspect that

the low-density layers are formed due to soft-sediment deformation (Allen, 1977), a process that would occur when the denser basaltic tephra sinks through the soft clay that is located at the top of the previous layer. This has been verified by analyzing the grainsize of the sediments in the affected area (Fig. 22), showing that a layer of higher grainsize is located underneath the low-grainsize layer. The top of high-grainsize underlaying layer was visually examined and proved to contain the tephra. Proving that the basaltic tephra had sunken through the clay in the top part of the layer.

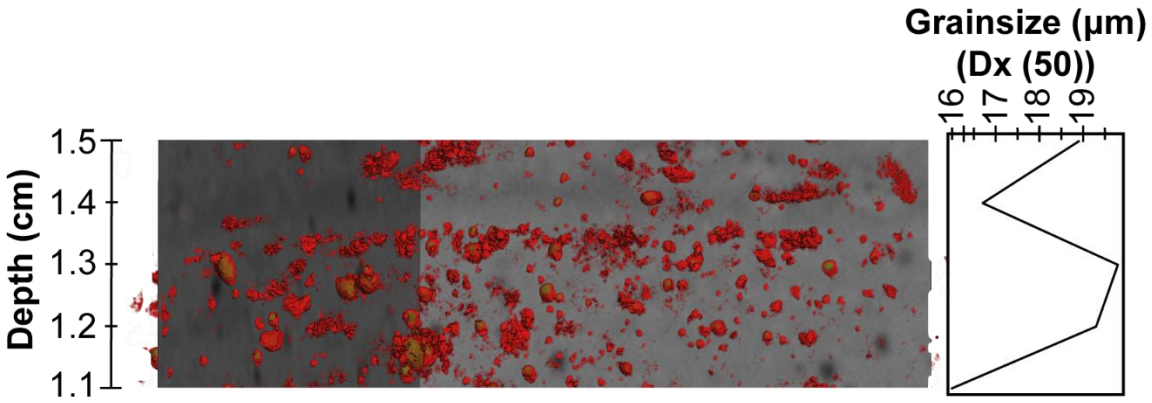

Figure 22 - Outcrop of second horizon of the synthetic core containing basalt aligned with the data from the Mastersizer (right side). As seen, there is a layer with higher grainsize in between two layers with lower grainsize. Visual inspection proved that the higher grainsize layer consist of tephra.

4.3 Application on real cores

4.3.1 DB2

The same two processes used on the synthetic organic cores were applied on the DB2-core. The latter core was spiked with a thin layer of rhyolitic tephra (top part; 95 cm) prior to scanning to use as calibration (section 4.1). *Volume Rendering* was then applied on the core, highlighting the grayscale values corresponding with the spiked horizon. As seen on figure 23, multiple areas correspond with the grayscale values of the spiked horizon. Thus, *SplineProbe* was also applied to try to further narrow down the areas containing tephra.

The *SplineProbe*-data shows three clear peaks (~100, ~108 and ~115 cm) (Fig. 21), and one clear trough (~108 cm). Using *Volume Rendering* it is possible to see that the peak at ~108 cm is due to a layer of sand (round clasts), and the trough at ~108 cm is due to a crack in the U-channel. When aligning the *SplinProbe*-data with the manual tephra counts from Oppedal et al. (2018) it correlate well (Fig. 24). The small offset between the clear peak at ~115 cm in the *SplineProbe*-data and the manual examination (peak at 112 cm) is believed to be due to tilting of the horizon as seen in figure 23, combined with the sampling interval of 1 cm used for the manual examination and a potential offset in depth when the U-channel was taken. The maximum tilting of the horizon at ~115 cm has been measured to 17,8 degrees to the horizontal using Avizo, meaning that if the tephra sampling was done ~7 cm away from the sampling of the U-channel the tilting alone could cause this offset. This is most likely to far away for the offset to be caused by the tilting alone, meaning that the sampling depth of the U-channel, as well as the counting interval of 1 cm most likely is a factor causing the offset.

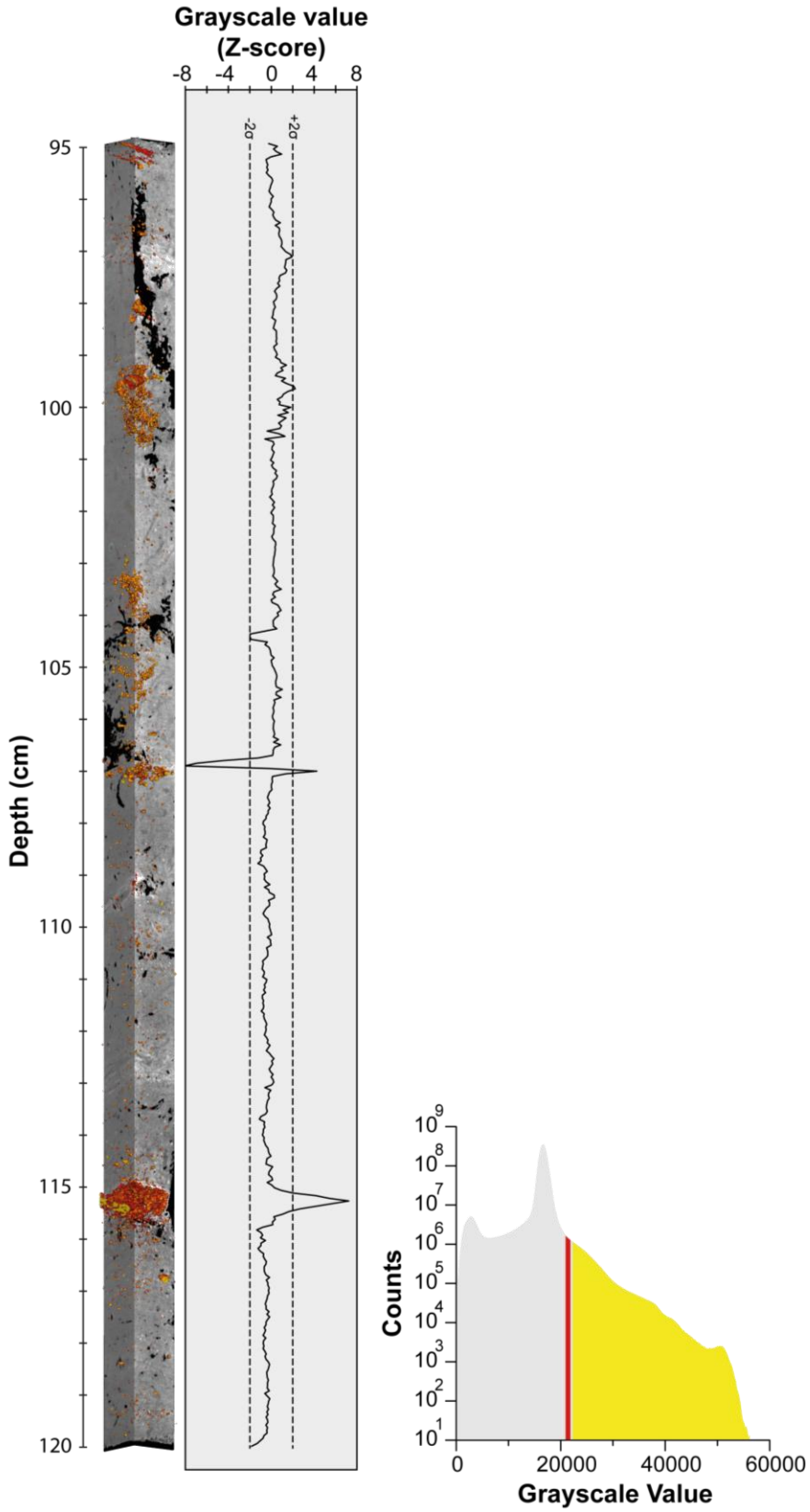

Figure 23 - Volume rendering of DB2 aligned with the normalized SplineProbe-graph. The yellow is sand, while the red is tephra (Grayscale value based on spiked horizon at 95 cm). As seen, there are three clear peaks in the graph (~100 cm, ~108 cm and ~115 cm). There are also one clear trough at ~108 cm, this is due to a crack in the core-section. The peak at ~108 is due to a layer of sand, visually confirmed by looking at the CT-data.

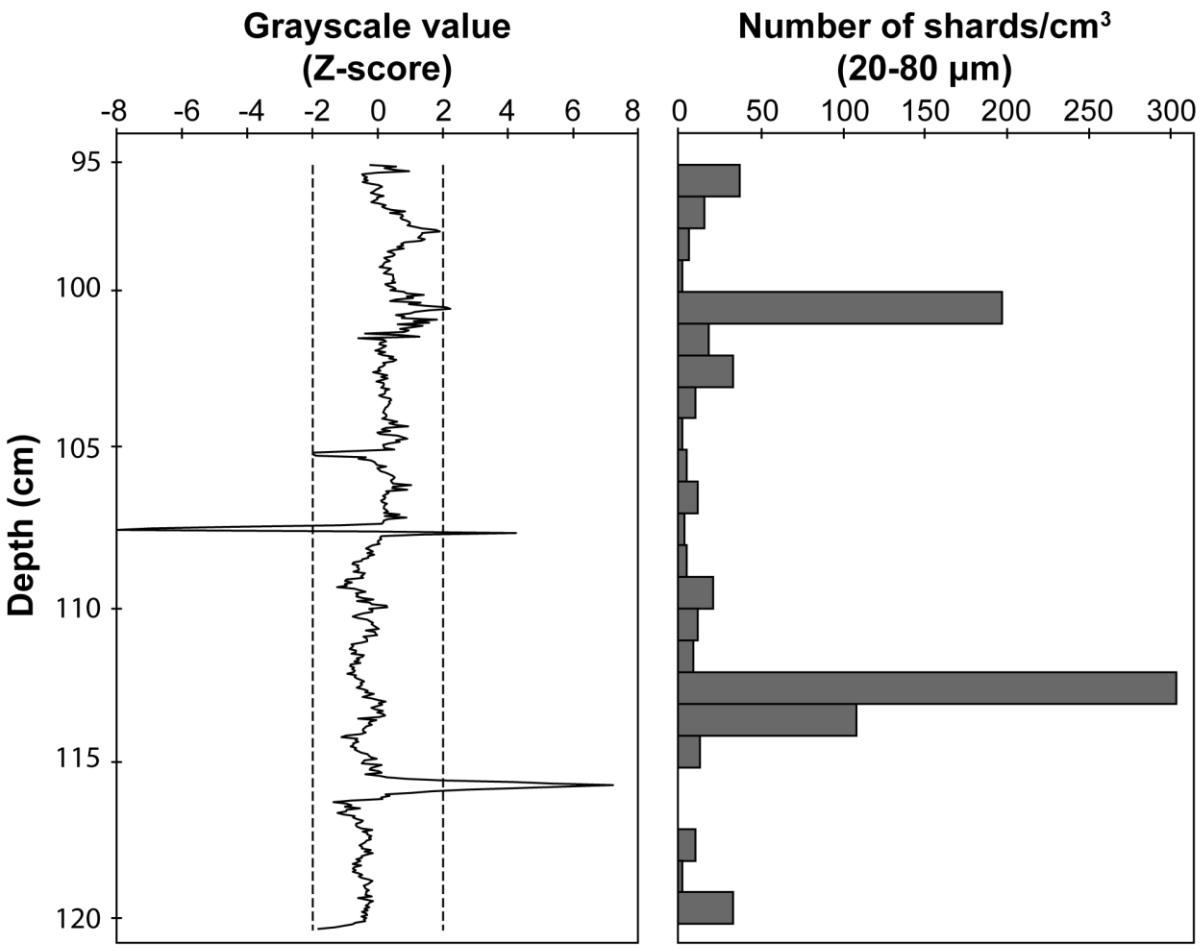

Figure 24 - Normalized SplineProbe-graph from DB2 aligned with the manual tephra counts from Oppedal et al. 2018. As seen, there are two peaks in the manual counts. The offset between the clear peak at ~115 cm and the manual counts is believed to be due to the counting interval (1 cm) and tilting of the layers (visually confirmed with CT scanning).

4.3.2 GS15-198-36CC

A 41 cm length of GS15-198-36CC was CT scanned. The area was chosen based on the current age-model for the core and the limitations regarding the processing computer (Section 3.6.1). Since the GS15-198-36CC core had not previously been examined for tephra, and is part of an ongoing research-project, we were not allowed to modify it in any way. This means that we could not spike it with a tephra horizon as was done with DB2. Based on the proximity to Iceland, the main tephra-type we were trying to locate was basaltic tephra. The method with manual interpretation of the grayscale distribution histogram and *Volume Rendering* was applied, isolating the same grayscale values in the histogram (relative to the matrix-peak) as for the basaltic synthetic core (Fig. 25). For GS15-198-36CC, ice rafted debris (IRD) was a major component. Large clasts (like IRD) have a higher grayscale value than smaller clasts of the same material since the middle of it does not get affected by the partial volume effect in the same way, thus IRD (sand) gets a higher grayscale value than silt and clay. However, the outer parts of a large clast will be affected by the partial volume effect (as seen on tephra horizon a in figure 17). Thus, for a core containing basaltic tephra and IRD with a silt/clay matrix the outer part of the IRD will end up with the same grayscale values as the basaltic tephra. To be able to distinguish the IRD from the potential tephra horizons the IRD was highlighted in yellow (Fig. 25), and it could then easily be identified based on the shape.

SplineProbe proved to be insufficient due to the high grayscale values of the surrounding sediments in the core (IRD). The focus was therefor on the *Volume Rendering*.

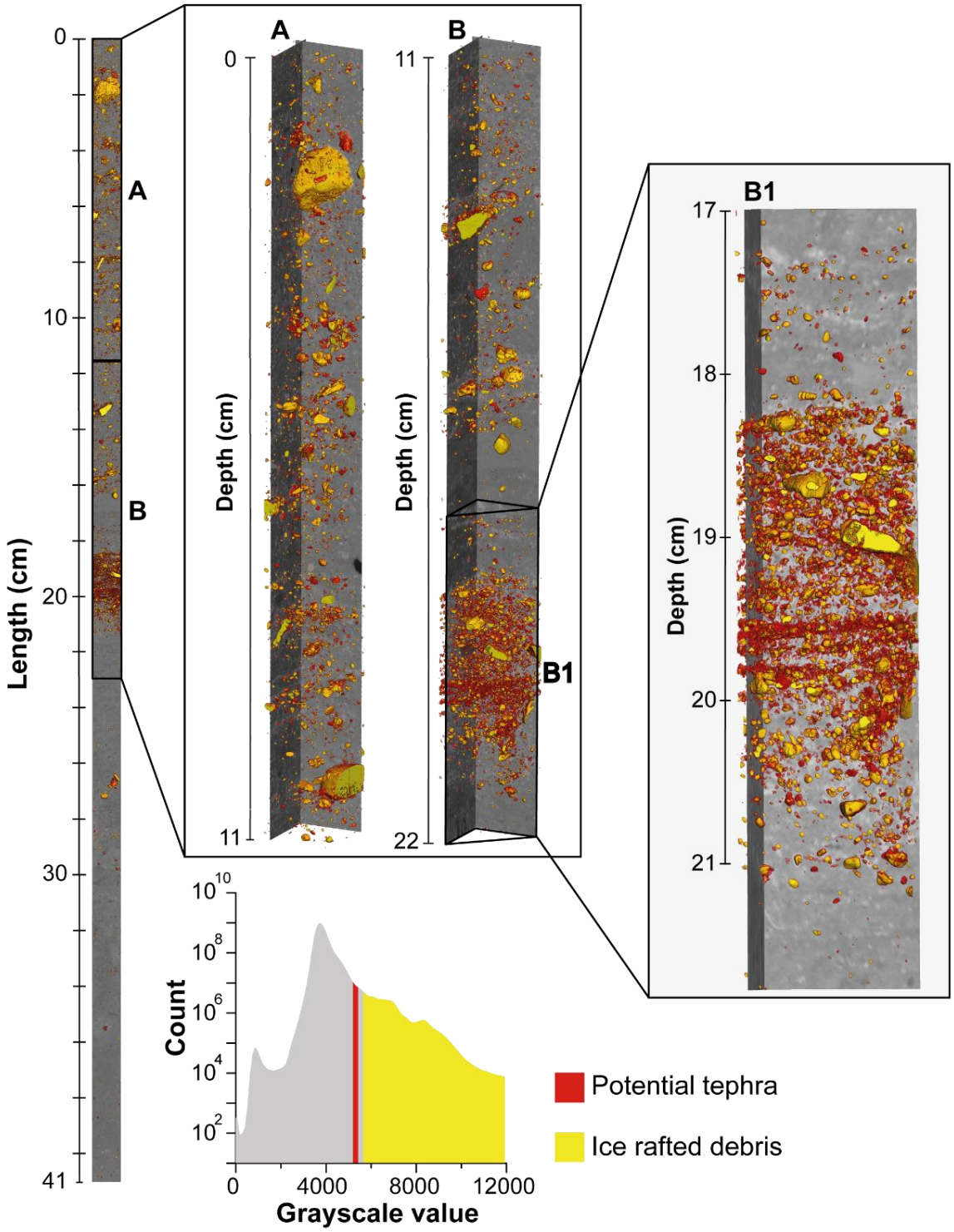

Figure 25 - Volume rendering of GS15-198-36CC, with potential tephra highlighted in red and IRD in yellow. Area A and B was most interesting as locations for tephra due to the high amount of material with the designated grayscale value in this area. The area B1 in section B was particularly interesting due to the three horizontal layers seemingly to contain tephra.

An area of interest was located 20 cm down in the core-section, with three compact layers with grayscale values within the designated range (Fig 25; B1 and Fig. 26). The three layers were visually looking like the tephra horizons previously found in the synthetic cores (Fig. 27). The core was afterwards manually examined based on the

CT scanning and processing done as part of this project (table 2), and it shows a peak in the tephra-counts in the predetermined area of interest (Fig 28).

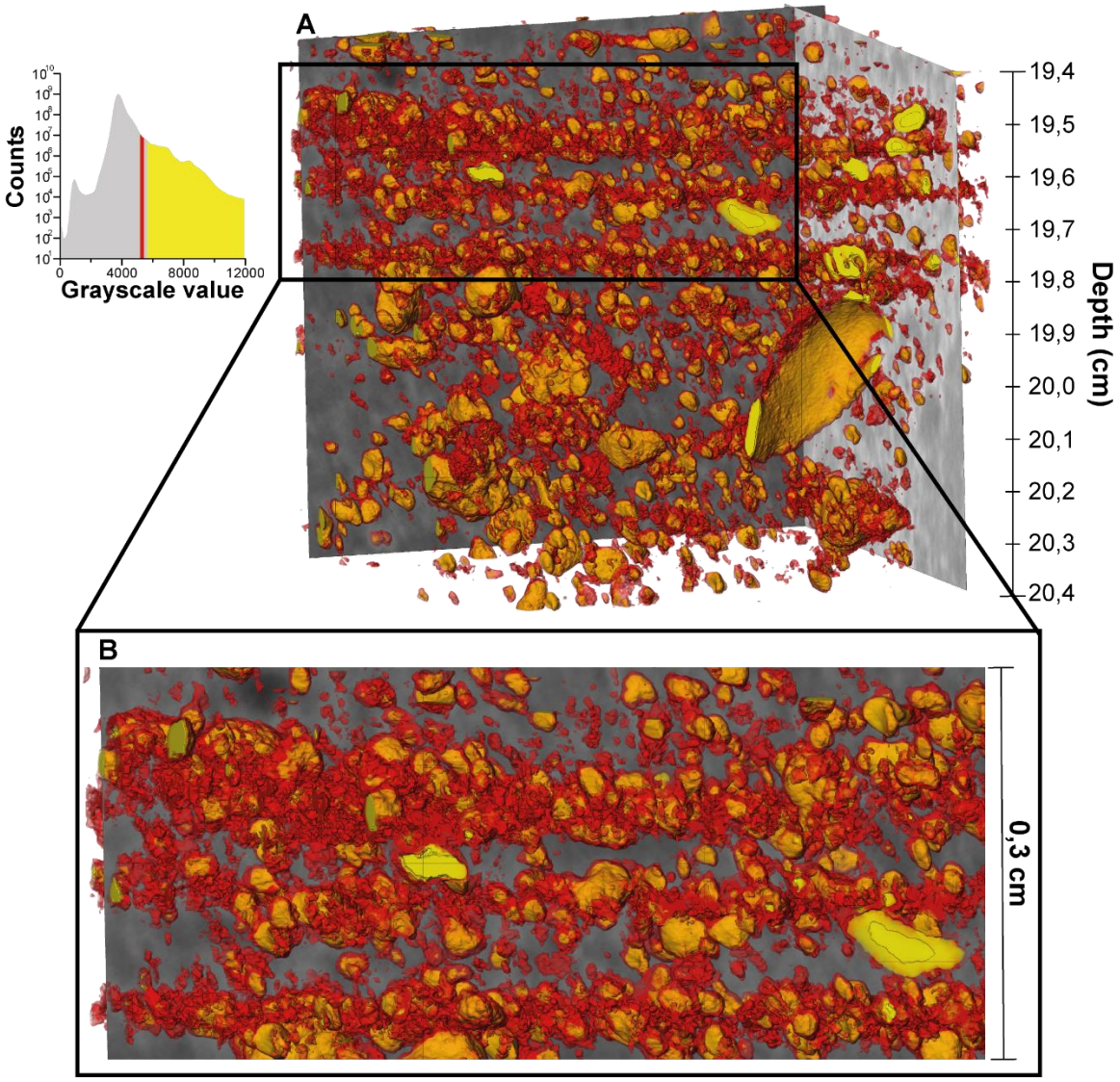

Figure 26 - Zoomed in on the area of interest in GS15-198-36CC (B1 in Fig. 25). Note the three horizontal red layers assumed to be tephra. Yellow spheres are interpreted as IRD.

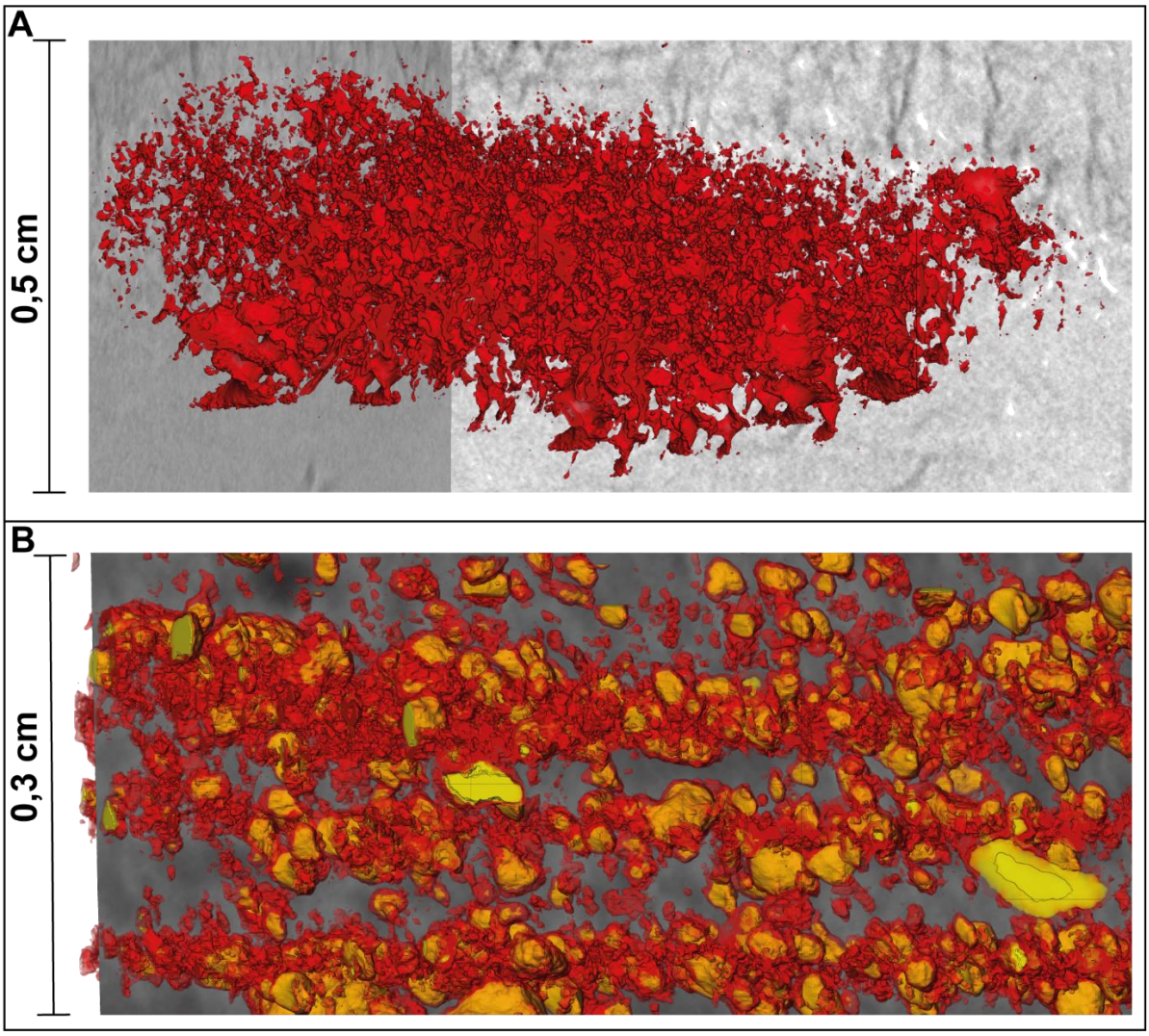

Figure 27 - Comparison of A) the basaltic tephra found in the synthetic ice core (Fig. 12) and B) the three distinct layers found in GS15-198-33CC (Fig. 26). As seen the texture is very much the same for the red area. Yellow spheres in B) is interpreted to be IRD based on grayscale value and shape.

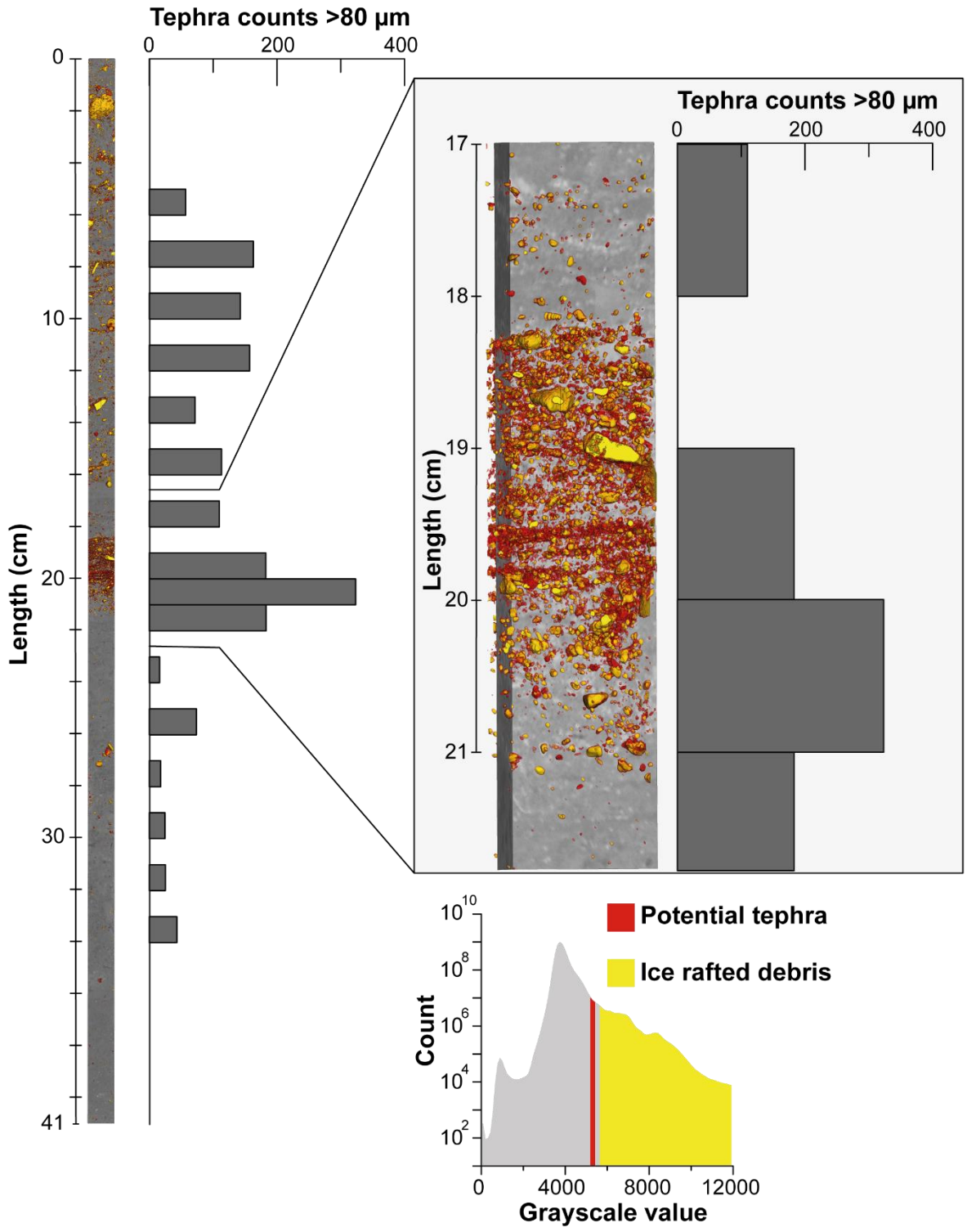

Figure 28 - Tephra counts for the whole section, and for the area of interest (B1 from Fig. 25) correlated with the volume rendering of the core. Note the three red layers corresponding well with the manual counts at 19,5 cm. The small offset is believed to be due to the counting interval (1 cm) and tilting layers.

In figure 28 a small offset of around 1 cm can be seen between the peak at 20,5 cm in the tephra counts and the three horizons seen at ~19,5 cm. This is believed to be due to the same reasons as in DB2 (Section 4.3.1); tilting and the sampling interval of 1 cm. Further, there is a low amount of tephra in the area below 22 cm, corresponding to the lack of material with the designated grayscale value in this area (Fig. 28). As no geochemical fingerprinting has been done, as for now, it is not possible to tell if there are three different eruption or one eruption causing the three horizons. For the area above the three horizons (0-19 cm) there is some lower tephra concentrations, corresponding with the appearance of volume rendered material with the designated grayscale value in this area.

5. Conclusion and implications

Based on the results in this study, we believe our method can be applied on sediment cores as part of the tephra-identification process. As the method involves some manual interpretation of the tephra horizons it requires training, and experience, in interpreting CT imagery. The method can also be more efficient if it is possible to spike the cores with a thin tephra horizon, as done on DB2.

As shown with the synthetic cores, the method works best in matrices with a lower density than the tephra (e.g. organic material or basaltic tephra in an minerogenic matrix). And the lower limit for how many tephra shards that can be detected relies highly on the matrix, as well as the lamination of the horizon, whereas vertical displacement of the tephra makes it harder to detect and can make the method insufficient. As the results also shows, the method has potential to not only identify areas of interest for further tephra analysis, but also more detailed information regarding the shape and occurrence of horizons. And as seen on GS15-198-36CC, with the occurrence of three horizons within an area that, using a normal sampling interval of 1 cm, would appear as one single horizon, it is possible to potentially improve tephrochronological frameworks. The fact that the process is non-destructive and can be applied without any implication on other lab-processes, and also allow for further CT processing of the scanned core (e.g. sediment structures (van der Bilt et al., 2018) and bioturbation impact on the tephra horizons (Rutledal et al., Submitted)), support the usage of the method.

This project highlights the problems related to the partial volume effect when CT scanning is applied in geoscience, and as seen it is important to take this effect into consideration when interpreting CT imagery.

6. Future work

By combining method using a CT scanner on a U-channel with the one from Griggs et al. (2015) and Evans et al. (2017), where they apply a microCT on even smaller samples to increase the resolution, we believe this can create a new, and better, understanding of how the tephra horizons are deposited and reworked. Their method will also limit the problem regarding the partial volume effect due to the higher resolution. In the future, it will most likely be possible to do high-resolution scans on whole core sections. The current limit is (for us) the fixed minimum distance between the core-holder and the source inside the CT scanner, and it should be technically possible to build a scanner that allows scanning of whole-length (1,5 m) U-channels with a resolution down to at least 10 µm. A CT scanner able to scan 1,5 m U-channels would require a high amount of computer-power, especially the amount of RAM required is high (Section 3.7), to be able to process the scans. The longest core-section used in this project is 41 cm long, with a file-size of 350 GB, giving a file-size of ~8,5 GB pr. cm. A 150 cm core with the same voxel size would thus give a file-size of approximately 1,2 TB. Processing this amount of data would require a custom-built computer made specific for this purpose with a higher amount of RAM than we currently have at EARTHLAB at the University of Bergen, and it would need to be even higher for a higher resolution scan. For the future, we believe that the ongoing innovation in computer-components will allow for high-resolution scans of full-length cores for a reasonable price, thus making CT scanning a more common method and allowing for further innovations regarding CT scanning in geoscience.

As seen in GS15-198-36CC, IRD can be easily spotted on a CT imagery, and thus we believe that there is a potential in the future for IRD-counting using CT scanning.

7. References

Abbott, Peter M., Griggs, Adam J., Bourne, Anna J. & Davies, Siwan M. (2018) Tracing marine cryptotephras in the North Atlantic during the last glacial period: Protocols for identification, characterisation and evaluating depositional controls. *Marine Geology,* 401**,** p. 81-97.

Allen, John R.L. (1977) The possible mechanics of convolute lamination in graded sand beds. *Journal of the Geological Society,* 134 (1)**,** p. 19-31.

Balascio, Nicholas L., Francus, Pierre, Bradley, Raymond S., Schupack, Benjamin B., Miller, Gifford H., Kvisvik, Bjørn C., Bakke, Jostein & Thordarson, Thorvaldur (2015) Investigating the Use of Scanning X-Ray Fluorescence to Locate Cryptotephra in Minerogenic Lacustrine Sediment: Experimental Results. *Micro-XRF Studies of Sediment Cores.* Springer, p. 305-324.

Bendle, Jacob M., Palmer, Adrian P. & Carr, Simon J. (2015) A comparison of micro-CT and thin section analysis of Lateglacial glaciolacustrine varves from Glen Roy, Scotland. *Quaternary Science Reviews,* 114**,** p. 61-77.

Biltema Norge (2017) HMS datablad 8_252134. 3 ed. Available from: http://www.biltema.no/no/Bat/Kjemikalier/Polyester-og-Epoksy/Lamineringsepoksy-2000020523/ [Accessed 25.08.2018]

Blockley, Simon P.E., Pyne-O'Donnell, Sean D. F., Lowe, John J., Matthews, Ian P., Stone, Abi, Pollard, A. Mark, Turney, Chris S. M. & Molyneux, Elizabeth G. (2005) A new and less destructive laboratory procedure for the physical separation of distal glass tephra shards from sediments. *Quaternary Science Reviews,* 24 (16-17)**,** p. 1952-1960.

Blockley, Simon P.E., Bourne, Anna J., Brauer, Achim, Davies, Siwan M., Hardiman, Mark, Harding, Poppy R., Lane, Christine S., MacLeod, Alison, Matthews, Ian P., Pyne-O'Donnell, Sean D. F., Rasmussen, Sune O., Wulf, Sabine & Zanchetta, Giovanni (2014) Tephrochronology and the extended intimate (integration of ice-core, marine and terrestrial records) event stratigraphy 8–128 ka b2k. *Quaternary Science Reviews,* 106**,** p. 88-100.

Bourne, Anna J., Cook, Eliza, Abbott, Peter M., Seierstad, Inger K., Steffensen, Jørgen Peder, Svensson, Anders, Fischer, Hubertus, Schüpbach, Simon & Davies, Siwan M. (2015) A tephra lattice for Greenland and a reconstruction of volcanic events spanning 25–45 ka b2k. *Quaternary Science Reviews,* 118**,** p. 122-141.

Brooks, Rodney A. & Di Chiro, Giovanni (1976) Beam hardening in x-ray reconstructive tomography. *Physics in medicine & biology,* 21 (3)**,** p. 390.

Bryant, JA, Drage, Nicholas A. & Richmond, Stephen (2012) CT number definition. *Radiation Physics and Chemistry,* 81 (4)**,** p. 358-361.

Compressed Gas Association (1999) *Handbook of compressed gases*, Springer Science & Business Media, p. 529

Davies, Siwan M. (2015) Cryptotephras: the revolution in correlation and precision dating. *Journal of Quaternary Science,* 30 (2)**,** p. 114-130.

Dugmore, Andrew (1989) Icelandic volcanic ash in Scotland. *Scottish Geographical Magazine,* 105 (3)**,** p. 168-172.

Dugmore, Andrew J., Newton, Anthony J., Smith, Kate T. & Mairs, Kerry-Ann (2013) Tephrochronology and the late Holocene volcanic and flood history of Eyjafjallajökull, Iceland. *Journal of Quaternary Science,* 28 (3)**,** p. 237-247.

Engineering ToolBox (2009). *Density of Selected Solids*. [online] Available at: https://www.engineeringtoolbox.com/density-solids-d_1265.html [Accessed 19.11.2019]

Evans, Elizabeth E., Davies, Siwan M. & Johnston, R.E. (2017). Phantom creation and analysis: Improving X-Ray microtomography scanning of soft sediment cores containing volcanic ash. *Journal of Physics: Conference Series*. IOP Publishing, 012012.

Feibel, Craig S. (1999) Tephrostratigraphy and geological context in paleoanthropology. *Evolutionary Anthropology: Issues, News, and Reviews: Issues, News, and Reviews,* 8 (3)**,** p. 87-100.

Fontijn, Karen, Lachowycz, Stefan M,. Rawson, Harriet, Pyle, David M., Mather, Tamsin A., Naranjo, José A & Moreno-Roa, Hugo (2014) Late Quaternary tephrostratigraphy of southern Chile and Argentina. *Quaternary Science Reviews,* 89**,** p. 70-84.

Gasser, Jürg A (2003) Bone measurements by peripheral quantitative computed tomography in rodents. *Bone research protocols.* Springer, p. 323-341.

Griggs, Adam J., Davies, Siwan. M., Abbott, Peter. M., Coleman, Mark, Palmer, Adrian P., Rasmussen, Tine L. & Johnston, Richard (2015) Visualizing tephra deposits and sedimentary processes in the marine environment: The potential of X-ray microtomography. *Geochemistry Geophysics Geosystems,* 16 (12)**,** p. 4329-4343.

Hayward, Chris (2011) High spatial resolution electron probe microanalysis of tephras and melt inclusions without beam-induced chemical modification. *The Holocene***,** p.119-125.

Hounsfield, Godfrey Newbold (1972) A method of and apparatus for examination of a body by radiation such as X-or gamma-radiation. *British Patent No. 1,283,915*.

Jansen, Eystein (2015) Cruise report of cruise GS15-198 (Reykjavik-Tromsø, July 19–August 15 2015).

Jensen, Britta J.L., Pyne-O'Donnell, Sean, Plunkett, Gill, Froese, Duane G., Hughes, Paul D.M., Sigl, Michael, McConnell, Joseph R., Amesbury, Matthew J., Blackwell, Paul G. & van den Bogaard, Christel (2014) Transatlantic distribution of the Alaskan white river ash. *Geology,* 42 (10)**,** p. 875-878.

Kalender, Willi A. (2011) *Computed tomography: fundamentals, system technology, image quality, applications*, Publicis MCD Verlag, Germany.

Lane, Christine S., Lowe, David J., Blockley, Simon P.E., Suzuki, Takehiko & Smith, Victoria C. (2017) Advancing tephrochronology as a global dating tool: Applications in volcanology, archaeology, and palaeoclimatology. *Quaternary Geochronology,* 40, p.1-7.

Lowe, David J. (2011) Tephrochronology and its application: a review. *Quaternary Geochronology,* 6 (2)**,** p. 107-153.

Oppedal, Lea T., van der Bilt, Willem G.M., Balascio, Nicholas L. & Bakke, Jostein (2018) Patagonian ash on sub-Antarctic South Georgia: expanding the tephrostratigraphy of southern South America into the Atlantic sector of the Southern Ocean. *Journal of Quaternary Science,* 33 (5)**,** p. 482-486.

Persson, Christer (1967) Försök till tefrokronologisk datering i tre norska myrar. *Geologiska Föreningen i Stockholm Förhandlingar,* 89 (2)**,** p. 181-197.

Petrovic, A. Martin, Siebert, James E. & Rieke, Paul E. (1982) Soil bulk density analysis in three dimensions by computed tomographic scanning. *Soil Science Society of America Journal,* 46 (3)**,** p. 445-450.

Poppe, Lawrence J., Paskevich, Valerie F., Hathaway, John C. & Blackwood, Dann S. (2001) A laboratory manual for X-ray powder diffraction*. US Geological Survey Open-File Repor*t 1.041**,** p. 1-88.

Razi, Tahmineh, Niknami, Mahdi & Ghazani, Fakhri Alavi (2014) Relationship between hounsfield unit in CT scan and gray scale in CBCT. *Journal of dental research, dental clinics, dental prospects,* 8 (2)**,** p. 107.
Renter, Jeroen A.M. (1989) Applications of computerized tomography in sedimentology. *Marine Georesources & Geotechnology,* 8 (3)**,** p. 201-211.
Rutledal, Sunniva, Berben, Sarah M.P., Dokken, Trond M., van der Bilt, Willem G.M., Cederstrøm, Jan M. & Jansen, Eystein (Submitted) Last Glacial tephra horizons identified in the western North Atlantic and Nordic Seas: Extending the marine tephra framework. *Quaternary Science Reviews*.
Røthe, Torgeir O., Bakke, Jostein & Støren, Eivind W.N. (2019) Glacier outburst floods reconstructed from lake sediments and their implications for Holocene variations of the plateau glacier Folgefonna in western Norway. *Boreas*. Vol. 48, p. 616–634.
Sessford, Evangelin G., Tisserand, Amandine A., Risebrobakken, Bjørg, Andersson, Carin, Dokken, Trond M. & Jansen, Eystein (2018) High-Resolution Benthic Mg/Ca Temperature Record of the Intermediate Water in the Denmark Strait Across D-O Stadial-Interstadial Cycles. *Paleoceanography and paleoclimatology,* 33 (11)**,** p. 1169-1185.
Smith, Victoria C., Staff, Richard A., Blockley, Simon P.E., Ramsey, Christopher B., Nakagawa, Takeshi, Mark, Darren F., Takemura, Keiji & Danhara, Toru (2013) Identification and correlation of visible tephras in the Lake Suigetsu SG06 sedimentary archive, Japan: chronostratigraphic markers for synchronising of east Asian/west Pacific palaeoclimatic records across the last 150 ka. *Quaternary Science Reviews,* 67**,** p. 121-137.
Souza, Andre, Udupa, Jayaram K. & Saha, Punam K. (2005) Volume rendering in the presence of partial volume effects. *IEEE transactions on medical imaging,* 24 (2)**,** p. 223-235.
Stevenson, John A., Loughlin, Susan, Rae, C., Thordarson, Thorvaldur, Milodowski, A.E., Gilbert, J.S., Harangi, Szabolcs, Lukács, Reka, Højgaard, Bartal & Árting, Uni (2012) Distal deposition of tephra from the Eyjafjallajökull 2010 summit eruption. *Journal of Geophysical Research: Solid Earth,* 117 (B9).
Støren, Eivind W.N., Dahl, Svein Olaf, Nesje, Atle & Paasche, Øyvind (2010) Identifying the sedimentary imprint of high-frequency Holocene river floods in lake sediments: development and application of a new method. *Quaternary Science Reviews,* 29 (23-24)**,** p. 3021-3033.
CT-Laboratory (2017) [Online]. uib.no: University of Bergen. Available: https://www.uib.no/en/geo/111536/ct-lab [Accessed 05.04.2019].
Thermo Fisher Scientific (2018) Thermo Scientific™ Avizo™ Software 9 - User's Guide.
Thorarinsson, Sigurdur (1944) Tefrokronologiska studier på Island: Þjórsárdalur och dess förödelse. *Geografiska annaler,* 26 (1-2)**,** p. 1-217.
Tomlinson, Emma L., Smith, Victoria C., Albert, Paul G., Aydar, Erkan, Civetta, Lucia, Cioni, Raffaello, Çubukçu, Evren, Gertisser, Ralf, Isaia, Roberto, Menzies, Martin A., Orsi, Giovanni, Rosi, Mauro & Zanchetta, Giovanni (2015) The major and trace element glass compositions of the productive Mediterranean volcanic sources: tools for correlating distal tephra layers in and around Europe. *Quaternary Science Reviews,* 118**,** p. 48-66.
Turney, Chris S.M. (1998) Extraction of rhyolitic component of Vedde microtephra from minerogenic lake sediments. *Journal of Paleolimnology,* 19 (2)**,** p. 199-206.

van der Bilt, Willem G.M., Lane, Christine S. & Bakke, Jostein (2017) Ultra-distal Kamchatkan ash on Arctic Svalbard: towards hemispheric cryptotephra correlation. *Quaternary Science Reviews,* 164**,** p. 230-235.
van der Bilt, Willem G.M., Rea, Brice, Spagnolo, Matteo, Roerdink, Desiree L., Jørgensen, Steffen L. & Bakke, Jostein (2018) Novel sedimentological fingerprints link shifting depositional processes to Holocene climate transitions in East Greenland. *Global and planetary change,* 164**,** p. 52-64.
Vinegar, Harold J. & Wellington, Scott L. (1986) Tomographic imaging of three-phase flow experiments. *Review of Scientific Instruments,* 58 (1)**,** p. 96-107.